Chemical Science

EDGE ARTICLE

View Article Online
View Journal | View Issue

Check for updates

Cite this: *Chem. Sci.*, 2023, **14**, 11890

All publication charges for this article have been paid for by the Royal Society of Chemistry

Surface engineering on a microporous metal–organic framework to boost ethane/ethylene separation under humid conditions†

Xiao-Jing Xie,[a] Ying Wang,[a] Qi-Yun Cao,[a] Rajamani Krishna,[b] Heng Zeng,*[a] Weigang Lu*[a] and Dan Li[a]

Recently, examples of metal–organic frameworks (MOFs) have been identified displaying ethane (C_2H_6) over ethylene (C_2H_4) adsorption selectivity. However, it remains a challenge to construct MOFs with both large C_2H_6 adsorption capacity and high C_2H_6/C_2H_4 adsorption selectivity, especially under humid conditions. Herein, we reported two isoreticular MOF-5 analogues (JNU-6 and JNU-6-CH_3) and their potential applications in one-step separation of C_2H_4 from C_2H_6/C_2H_4 mixtures. The introduction of CH_3 groups not only reduces the pore size from 5.4 Å in JNU-6 to 4.1 Å in JNU-6-CH_3 but also renders an increased electron density on the pyrazolate N atoms of the organic linker. JNU-6-CH_3 retains its framework integrity even after being immersed in water for six months. More importantly, it exhibits large C_2H_6 adsorption capacity (4.63 mmol g^{-1}) and high C_2H_6/C_2H_4 adsorption selectivity (1.67) due to the optimized pore size and surface function. Breakthrough experiments on JNU-6-CH_3 demonstrate that C_2H_4 can be directly separated from C_2H_6/C_2H_4 (50/50, v/v) mixtures, affording benchmark productivity of 22.06 and 18.71 L kg^{-1} of high-purity C_2H_4 (≥99.95%) under dry and humid conditions, respectively.

Received 7th August 2023
Accepted 8th October 2023

DOI: 10.1039/d3sc04119k

rsc.li/chemical-science

As one of the seven world-changing chemical separations, olefin/paraffin separation accounts for more than 0.3% of global energy consumption.[1] Ethylene (C_2H_4) is an important chemical feedstock in petrochemical industries, with a global production capacity of over 200 million tons in 2023.[2] At present, C_2H_4 is mainly produced *via* steam cracking of ethane (C_2H_6) in industry, which would inevitably leave a certain amount of C_2H_6 in the obtained C_2H_4. Given that the C_2H_6 impurity may interfere with the polymerization process, further purification is required and the polymer-grade (≥99.95%) C_2H_4 is highly desired in the manufacture of value-added chemicals. Owing to their very similar physicochemical properties and molecular sizes ($3.81 \times 4.08 \times 4.82$ Å^3 and $3.28 \times 4.18 \times 4.84$ Å^3 for C_2H_6 and C_2H_4, respectively), the industrial C_2H_4/C_2H_6 separation relies on cryogenic distillation, which is energy intensive and requires high distillation towers with many trays in order to achieve high reflux ratios.[3]

Compared to traditional distillation, non-thermal separation technologies using porous materials are of great significance to energy-efficient separation economy.[4,5] Metal–organic frameworks (MOFs), also known as porous coordination polymers (PCPs),[6–8] have been extensively investigated in hydrocarbon separation due to their highly tunable pore geometry and surface chemistry. With regard to C_2H_4/C_2H_6 separation, MOFs can be categorized into two types: C_2H_6-selective and C_2H_4-selective. For C_2H_4-selective MOFs, desorption by heat or purge is necessary in order to obtain C_2H_4, which likely would result in C_2H_6 contamination. For example, the benchmark C_2H_4/C_2H_6 sieving MOF, UTSA-280,[9] can realize complete exclusion of large-sized C_2H_6 molecules and an infinite C_2H_4 over C_2H_6 selectivity, yet C_2H_4 with only 99.1% purity was reported upon desorption.

By contrast, C_2H_6-selective MOFs allow for direct production of C_2H_4 in a single adsorption step, which could potentially save *ca.* 40% of energy consumption (0.4 to 0.6 GJ ton^{-1} of C_2H_4) for C_2H_4/C_2H_6 separation.[10] Considering the numbers of hydrogen atoms on the surface of C_2H_6 and C_2H_4 molecules (6 *vs.* 4), controlled surface engineering with polar functions (*e.g.*, N- and O-containing groups) on the pore walls may facilitate non-classic hydrogen bonding and stronger affinity toward C_2H_6 than C_2H_4.[5,11–16] Nevertheless, water vapor may compete for the interactions with those polar functional groups, leading to substantially reduced separation potential under humid

---

[a] *College of Chemistry and Materials Science, Guangdong Provincial Key Laboratory of Functional Supramolecular Coordination Materials and Applications, Jinan University, Guangzhou 510632, P. R. China. E-mail: zengheng90@163.com; weiganglu@jnu.edu.cn*

[b] *Van't Hoff Institute for Molecular Sciences, University of Amsterdam, Science Park 904, Amsterdam 1098 XH, Netherlands*

† Electronic supplementary information (ESI) available. CCDC 2258075, 2286047 and 2259108. For ESI and crystallographic data in CIF or other electronic format see DOI: **https://doi.org/10.1039/d3sc04119k**

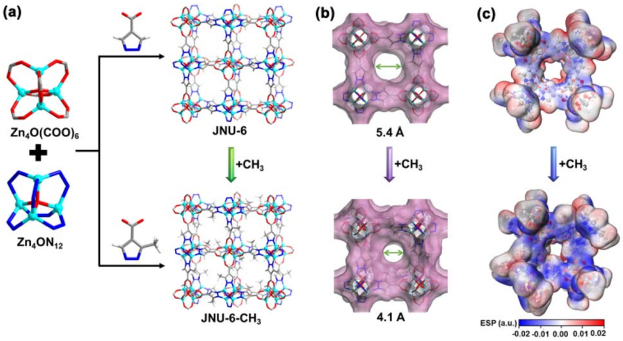

Fig. 1 (a) Isostructural frameworks of JNU-6 and JNU-6-CH_3 assembled with two six-connected Zn_4O SBUs and their respective organic linkers. (Color code: Zn, cyan; C, dark gray; N, blue; O, red; H, white). (b) Connolly surface analysis of JNU-6 and JNU-6-CH_3, depicting the reduced pore size upon the introduction of CH_3 groups. (c) Electrostatic potential mapping of JNU-6 and JNU-6-CH_3, depicting the increased electron density on pyrazolate N atoms upon the introduction of CH_3 groups.

conditions. For example, the benchmark C_2H_6-selective MOF, $Fe_2(O_2)(dobdc)$,[17] demonstrated an excellent C_2H_6 over C_2H_4 selectivity with a record separation factor of *ca.* 4.4. The material itself, however, is extremely sensitive to moisture and has to be handled in a glove box. Recent studies show that nonpolar pore environments can prevent moisture from entering inside the frameworks and therefore retain the C_2H_4/C_2H_6 separation potential even under humid conditions. More importantly, nonpolar pore surfaces may still facilitate C_2H_6 over C_2H_4 selectivity due to their slightly different polarizability (C_2H_6: 44.7×10^{25} cm^3, C_2H_4: 42.5×10^{25} cm^3). For instance, the MOF FJI-H11-Me-(des),[18] featuring nonpolar pore surfaces comprised of aromatic rings and alkyl groups, exhibits a stable C_2H_6 over C_2H_4 separation capacity in a wide range of relative humidities (RHs). However, the overall separation potential was limited due to its moderate adsorption capacity for C_2H_6 (2.58 mmol g^{-1}). Until now, it remains a challenge to construct MOFs with both large C_2H_6 adsorption capacity and high C_2H_6 over C_2H_4 adsorption selectivity to break the adsorption/selectivity trade-off limitation, especially under humid conditions.

Isoreticular chemistry allows for the design and synthesis of MOFs with tailor-made pore dimensions and functions for selective binding of one over the other in C_2H_4/C_2H_6 separation. The methyl (CH_3) group is electron-donating, and its effect on gas adsorption and separation has been well documented.[19–21] In addition, the CH_3 group is considered strongly hydrophobic, and the MOF decorated with CH_3 groups usually exhibits low water adsorption capacity even at high RH, which could effectively suppress the competition of water vapor for adsorption sites. Herein, we selected $Zn_4O(PyC)_3$ (termed here as JNU-6, H_2PyC = pyrazole-4-carboxylic acid), an isoreticular MOF-5 analogue,[22–24] as the platform for surface functionalization *via* linker methylation. We found that the introduction of CH_3 groups not only reduces the pore size from 5.4 Å in JNU-6 to 4.1 Å in JNU-6-CH_3 but also renders an increased electron density on the pyrazolate N atoms of the organic linker. As a result, JNU-6-CH_3 retains its framework integrity even after being immersed in water for six months. More importantly, it exhibits large C_2H_6 adsorption capacity (4.63 mmol g^{-1}) and high C_2H_6/C_2H_4 adsorption selectivity (1.67) due to the optimized pore size and surface function. Breakthrough experiments on JNU-6-CH_3 demonstrate benchmark productivity of 22.06 and 18.71 L kg^{-1} of high-purity $\mathbf{C_2H_4}$ (≥99.95%) from a C_2H_6/C_2H_4 (50 : 50) mixture under dry and humid conditions, respectively.

To apply reticular chemistry and address the separation challenge of C_2H_6/C_2H_4 under humid conditions, it is crucial to find a C_2H_6-selective MOF that can be easily functionalized. In this work, we selected an isoreticular analogue of MOF-5 as the platform for the introduction of CH_3 groups. A solvothermal reaction of $Zn(NO_3)_2$ with pyrazole-4-carboxylic acid or 3-methylpyrazole-4-carboxylic acid in a mixed solution of DEF/H_2O afforded high-quality block crystals of JNU-6 and JNU-6-CH_3, respectively. Single crystal X-ray diffraction (SCXRD) analyses reveal that JNU-6 and JNU-6-CH_3 are of cubic crystal structure isoreticular to MOF-5. It should be pointed out that both JNU-6 and JNU-6-CH_3 were reported by Zhong and co-workers recently for n-C_4H_{10}/iso-C_4H_{10} separation during our preparation of this paper.[25] In the crystal structures, two types of octahedral Zn_4O SBUs (secondary building units, Zn_4ON_{12} and $Zn_4O(COO)_6$) are connected by ditopic organic linkers to form a 3-dimensional (3D) network with interconnected cubic-shaped cages (Fig. 1a). The introduction of CH_3 groups on the pore surface decreases the aperture size from 5.4 Å to 4.1 Å (Fig. 1b), making it more comparable to the kinetic diameters of C_2H_6 and C_2H_4 (C_2H_6 = 4.44 Å, C_2H_4 = 4.16 Å).[26] Density functional theory (DFT) calculations were carried out to generate the mapping of electrostatic potential (ESP) on JNU-6 and JNU-6-CH_3. As shown in Fig. 1c, an increased electron density was observed on the pyrazole rings of JNU-6-CH_3, particularly around the N atoms, owing to the electron-donating effect of the CH_3 groups. Such an electrostatic potential in JNU-6-CH_3 indicates an increased surface dipole, which may potentially facilitate the discrimination of C_2H_6 from C_2H_4 due to their slightly different polarizability.

The phase purity and crystallinity of the bulk JNU-6 and JNU-6-CH_3 samples were checked by powder X-ray diffraction (PXRD) analyses, showing good agreement with the ones simulated from their respective crystal structures. N_2 adsorption/desorption isotherms at 77 K were measured to investigate the porosity of JNU-6 and JNU-6-CH_3. As shown in Fig. 2a, both of them exhibit type-I adsorption/desorption isotherms characteristic of microporous materials. Due to the introduction of CH_3 groups, the calculated Brunauer–Emmett–Teller (BET) surface area of JNU-6-CH_3 is slightly decreased from 1411 m^2 g^{-1} in JNU-6 to 1270 m^2 g^{-1}, and the calculated pore volume is also decreased from 0.59 cm^3 g^{-1} in JNU-6 to 0.51 cm^3 g^{-1}. Further, the pore size distribution was determined by the Horvath–Kawazoe model and the dominant pore diameters exhibit the same trend, with values decreasing from 5.4 Å in JNU-6 to 4.1 Å in JNU-6-CH_3 (Fig. 2a, inset).

Single-component adsorption isotherms of JNU-6 and JNU-6-CH_3 for C_2H_6 and C_2H_4 were measured at 298 K. As exhibited in Fig. 2b, the C_2H_6 adsorption capacity is substantially larger than C_2H_4 in the entire pressure range (0–1 bar) for both JNU-6 and

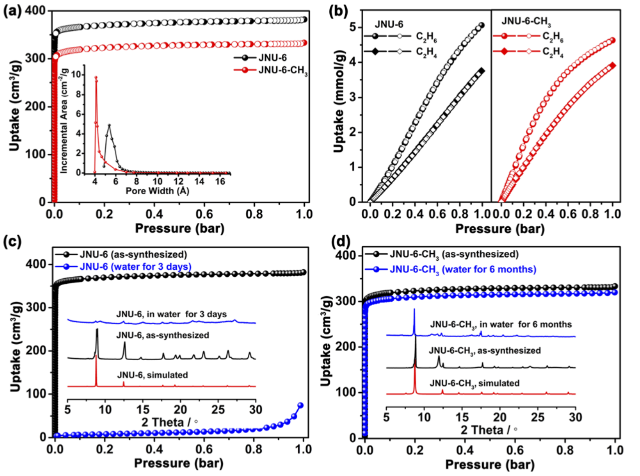

Fig. 2 (a) N_2 adsorption/desorption isotherms of JNU-6 and JNU-6-CH_3 at 77 K. Inset shows the difference in their pore size distribution. (b) C_2H_6 and C_2H_4 adsorption/desorption isotherms of JNU-6 and JNU-6-CH_3 at 298 K. (c) Comparison of N_2 adsorption isotherms at 77 K and PXRD patterns of the as-synthesized JNU-6 and water-treated JNU-6 (being soaked in water for 3 days). (d) Comparison of N_2 adsorption isotherms at 77 K and PXRD patterns of the as-synthesized JNU-6-CH_3 and water-treated JNU-6-CH_3 (being soaked in water for 6 months).

JNU-6-CH_3. The maximum uptakes for C_2H_4 are 84.4 cm^3 g^{-1} (3.77 mmol g^{-1}) and 88.1 cm^3 g^{-1} (3.93 mmol g^{-1}) on JNU-6 and JNU-6-CH_3, respectively, while the uptakes for C_2H_6 can reach up to 113.6 cm^3 g^{-1} (5.07 mmol g^{-1}) and 103.7 cm^3 g^{-1} (4.63 mmol g^{-1}) on JNU-6 and JNU-6-CH_3, respectively. The C_2H_6 uptakes on JNU-6 and JNU-6-CH_3 are comparable to or larger than those of most of the C_2H_6-selective MOFs, such as Cu(Qc)$_2$ (1.84 mmol g^{-1}),[27] MUF-15 (4.69 mmol g^{-1}),[28] NKMOF-8-Br (4.22 mmol g^{-1}),[29] FJI-H11-Me-(des) (2.58 mmol g^{-1}),[18] Ni(IN)$_2$ (3.05 mmol g^{-1}),[30] AzoleTh-1 (4.47 mmol g^{-1}),[31] and NPU-1 (4.5 mmol g^{-1}).[32] We applied the ideal adsorbed solution theory (IAST) to calculate the adsorption selectivity, and the IAST selectivity of JNU-6-CH_3 for a C_2H_6/C_2H_4 (50 : 50) mixture at 298 K can reach up to 1.67 (Fig. S4–S9†), which is comparable to those of the reported benchmark MOF adsorbents, such as MUF-15 (1.96),[28] NKMOF-8-Br (2.65),[29] NKMOF-8-Me (1.88),[29] Ni(IN)$_2$ (2.44),[30] AzoleTh-1 (1.46),[31] and NPU-1 (1.32).[32] Isosteric heat of adsorption (Q_{st}) was calculated by fitting adsorption isotherms at 273, 283, and 298 K using the dual-site Langmuir–Freundlich model (Fig. S10–S19†). At 298 K, the Q_{st} of JNU-6 at zero loading was determined to be 24.0 kJ $mol^{-1}$and 20.9 kJ mol^{-1} for C_2H_6 and C_2H_4, respectively, while the Q_{st} of JNU-6-CH_3 at zero loading was determined to be 24.7 kJ mol^{-1} *vs.* 23.9 kJ mol^{-1} for C_2H_6 and C_2H_4, respectively. The data confirm the stronger thermodynamic affinity toward C_2H_6 than C_2H_4 in both materials. Moreover, the reduced pore size in JNU-6-CH_3 may allow for an increased host–guest interaction between the framework and gas molecules, resulting in adsorption affinity stronger than JNU-6 for both C_2H_6 and C_2H_4. Meanwhile, the Q_{st} values of both JNU-6 and JNU-6-CH_3 are much lower than those of $Fe_2(O_2)$(dobdc) (67 kJ mol^{-1}),[17] IRMOF-8 (52.5 kJ mol^{-1}),[33] PAF-40-Fe (47.8 kJ mol^{-1}),[34] Zn-atzipa (45.8 kJ mol^{-1}),[35] and MAF-49 (60 kJ mol^{-1}).[12] The relatively low Q_{st} value may facilitate easy regeneration and low energy consumption during the desorption process, reflecting the advantages of pore surface engineering with nonpolar functional groups. Furthermore, ten continuous adsorptions for C_2H_6 and C_2H_4 were carried out on an ASAP2020 gas sorption instrument. As shown in Fig. S20–S23,† both JNU-6 and JNU-6-CH_3 retain adsorption capacity over ten cycles, indicating that the samples can be fully regenerated by vacuum at room temperature.

To test their water stability, JNU-6 and JNU-6-CH_3 were soaked in water for days and then subjected to PXRD and gas adsorption measurements. As shown in Fig. 2c, JNU-6 lost most of the crystallinity and porosity after being soaked in water for three days. In contrast, the crystallinity and structural integrity of JNU-6-CH_3 can be well retained after being soaked in water for six months (Fig. 2d). Water vapor adsorption measurements for JNU-6 and JNU-6-CH_3 were carried out and both of them show S-shaped adsorption isotherms characteristic of pore filling (Fig. 4b), and the limited water uptake at low pressure suggests that the water affinity on the MOF surface is relatively low. With the linker methylation, higher water vapor pressure is required to induce the pore filling, indicating further increased hydrophobicity of MOF pores from JNU-6 and JNU-6-CH_3. Overall, the introduction of CH_3 groups renders JNU-6-CH_3 with an optimized pore size, increased surface dipole, and improved hydrolytic stability, which prompted us to further study its potential for C_2H_6/C_2H_4 separation under humid conditions.

To verify the preferential adsorption of C_2H_6 over C_2H_4 on JNU-6 and JNU-6-CH_3, we first performed computational modeling studies using grand canonical Monte Carlo (GCMC) simulations.[35,36] The simulated C_2H_6 and C_2H_4 adsorption isotherms are in good agreement with the experimental ones at 298 K and 1 bar, and the probability density distributions of C_2H_6 and C_2H_4 reveal that both C_2H_6 and C_2H_4 are preferentially adsorbed at the corners of the cubic-shaped cages in both JNU-6 and JNU-6-CH_3 (Fig. S24–S27†). Take JNU-6-CH_3 as an example, there are six C–H···π interactions between the H atoms of C_2H_6 and the pyrazole rings of the linkers with H···π distances from 2.93 to 3.41 Å. In comparison, there are fewer C–H···π interactions between C_2H_4 and the pyrazole rings of the linkers with H···π distances from 3.0 to 3.85 Å (Fig. 3b and e). Further, an independent gradient model based on Hirshfeld partition (IGMH) analysis on the optimized structures was developed. As shown in Fig. 3c and f, multiple green isosurfaces were observed for both C_2H_6 and C_2H_4, indicating the existence of vdW interactions between the gas molecules and the three pyrazole rings. The static binding energies (ΔE) for C_2H_6 on JNU-6 and JNU-6-CH_3 were calculated to be 18.04 and 22.23 kJ mol^{-1}, respectively, higher than those for C_2H_4 (17.22 and 20.15 kJ mol^{-1}). These values further confirm the weak vdW nature of the host–guest interactions between gas molecules and the nonpolar pore surfaces, which favors the adsorption of C_2H_6 over C_2H_4.

To evaluate the actual separation capability of JNU-6 and JNU-6-CH_3 for C_2H_6/C_2H_4 mixtures, we first performed dynamic column breakthrough experiments in which a C_2H_6/C_2H_4 (50/

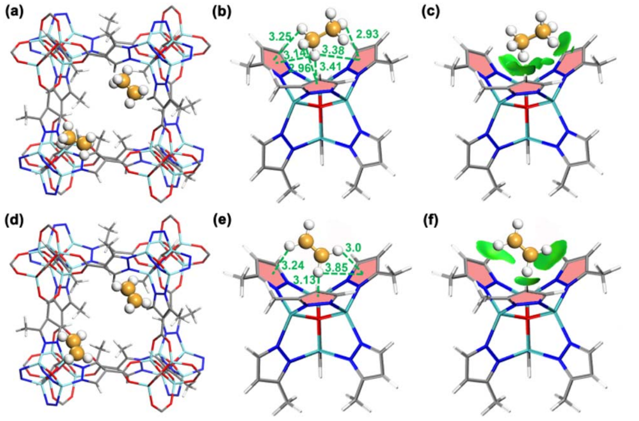

Fig. 3 Primary adsorption sites for C_2H_6 (a) and C_2H_4 (d) in JNU-6-CH_3 determined by Monte Carlo (GCMC) simulations. C–H⋯π interactions (green dashed lines) for C_2H_6 (b) and C_2H_4 (e) at the primary adsorption site of JNU-6-CH_3. Independent gradient model based on Hirshfeld partition (IGMH) analysis for C_2H_6 (c) and C_2H_4 (f) at the primary adsorption site of JNU-6-CH_3 (green surfaces represent vdW interactions). (Color code: Zn, cyan; C, dark gray; N, blue; O, red; H, white. The distance unit is in Å).

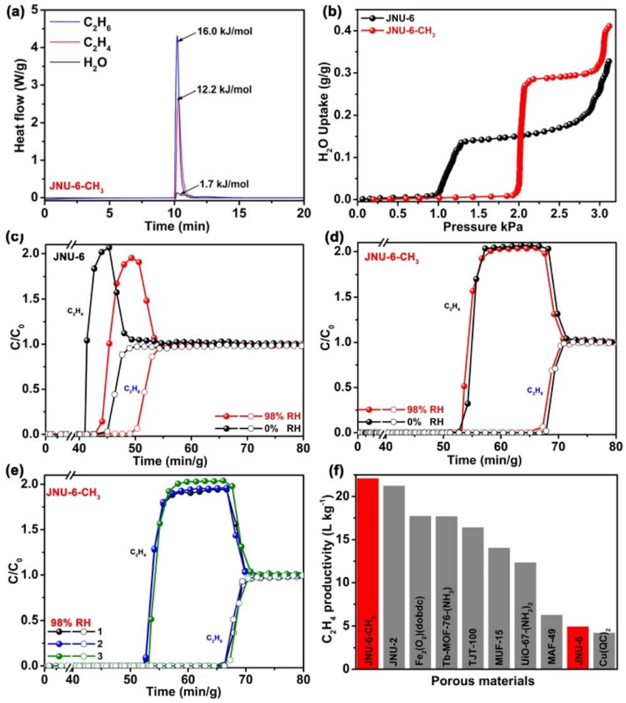

Fig. 4 (a) Differential scanning calorimetry (DSC) measurements of heat flow upon introducing C_2H_6, C_2H_4, and water vapor on JNU-6-CH_3 at a flow rate of 10 mL min^{-1} at 298 K. (b) Water vapor adsorption isotherms of JNU-6 and JNU-6-CH_3 at 298 K. (c) Experimental breakthrough curves on JNU-6 (1.0 g) for a C_2H_6/C_2H_4 (50/50, v/v) mixture at a flow rate of 2.0 mL min^{-1} and 298 K under 0% RH and 98% RH conditions. (d) Experimental breakthrough curves on JNU-6-CH_3 (0.85 g) for a C_2H_6/C_2H_4 (50/50, v/v) mixture at a flow rate of 2.0 mL min^{-1} and 298 K under 0% RH and 98% RH conditions. (e) Three cycles of breakthrough experiments on JNU-6-CH_3 for a C_2H_6/C_2H_4 (50/50, v/v) mixture at a flow rate of 2.0 mL min^{-1} and 298 K under 98% RH conditions. (f) Comparison of the C_2H_4 productivity estimated from breakthrough curves for JNU-6-CH_3, JNU-6, and other reported porous materials.

50, v/v) mixture was introduced over the activated JNU-6 or JNU-6-CH_3 at a flow rate of 2 mL min^{-1} and 298 K. As shown in Fig. 4c, JNU-6 can separate C_2H_6 from the C_2H_6/C_2H_4 mixture with an estimated productivity of 4.92 L kg^{-1} of high-purity C_2H_4 (≥99.95%) under dry conditions. Surprisingly, JNU-6-CH_3 exhibits significantly improved separation capacity under similar conditions, and the data are in good agreement with the simulated breakthrough curve (Fig. S29†). As shown in Fig. 4d, C_2H_4 and C_2H_6 were detected to break through the column at the time points of 52.7 min g^{-1}and 67.9 min g^{-1}, respectively. During the above time period, high-purity C_2H_4 (≥99.95%) can be collected with an estimated C_2H_4 productivity of 22.06 L kg^{-1}, which is about four times that of JNU-6 and the highest among those of the reported MOFs under similar conditions, including JNU-2 (21.2 L kg^{-1}),[13] $Fe_2(O_2)$(dobdc) (17.7 L kg^{-1}),[17] Tb-MOF-76-(NH_2) (17.66 L kg^{-1}),[37] TJT-100 (16.38 L kg^{-1}),[38] MUF-15 (14 L kg^{-1}),[28] UiO-67-$(NH_2)_2$ (12.32 L kg^{-1}),[5] MAF-49 (6.23 L kg^{-1}),[12] and $Cu(Qc)_2$ (4.0 L kg^{-1})[27] (Fig. 4f).

To further examine the moisture effect on the separation capability for C_2H_6/C_2H_4, we performed differential scanning calorimetry (DSC) measurements of heat flow upon introducing water vapor, C_2H_4, and C_2H_6 on JNU-6 and JNU-6-CH_3. For JNU-6, the experimental Q_{st} for water vapor, C_2H_4, and C_2H_6 is 0.2, 10.2, and 15.7 kJ mol^{-1}, respectively (Fig. S38†), while for JNU-6-CH_3, the experimental Q_{st} for water vapor, C_2H_4, and C_2H_6 is 1.7, 12.2, and 16.0 kJ mol^{-1}, respectively (Fig. 4a), both indicative of significantly stronger binding affinity for C_2H_6 and C_2H_4 than for water vapor. This, together with water vapor adsorption measurements (Fig. 4b), suggests that JNU-6-CH_3 may be able to maintain the high separation capability for C_2H_6/C_2H_4 mixtures under humid conditions. Breakthrough experiments were thus performed on JNU-6 and JNU-6-CH_3 for a C_2H_6/C_2H_4 (50/50, v/v) mixture under 98% RH conditions. As revealed in Fig. 4c and d, the purity of C_2H_4 dropped from 99.95% to 99.2% for JNU-6, likely due to its hydrolytic instability (Fig. 2c), whereas the purity of C_2H_4 remained over 99.95% with only slightly dropped productivity (18.71 L kg^{-1}) for JNU-6-CH_3. The results confirm that the introduction of CH_3 groups in the framework can indeed improve separation capability, especially under humid conditions. Furthermore, continuous breakthrough experiments under humid conditions were carried out, revealing the retained separation performance of JNU-6-CH_3 over three cycles (Fig. 4e and S31†).

To further study the effect of methylation degree on adsorption separation performance, we synthesized JNU-6-$(CH_3)_2$ with 3,5-dimethylpyrazole-4-carboxylic acid. JNU-6-$(CH_3)_2$ also shows preferential adsorption of C_2H_6 over C_2H_4, especially in the low-pressure range (Fig. S33†). However, its C_2H_6 and C_2H_4 adsorption amounts at 0.5 bar are almost the same, and the adsorption of C_2H_6 and C_2H_4 on JNU-6-$(CH_3)_2$ is significantly lower than those on JNU-6-CH_3 and JNU-6 in the high-pressure range, likely due to the reduced porosity of JNU-6-$(CH_3)_2$ (Fig. S32a†). As a result, dynamic column breakthrough experiments on JNU-6-$(CH_3)_2$ reveal a poor separation for a C_2H_6/C_2H_4 (50/50, v/v) mixture at a flow rate of 2.0 mL min^{-1}

and 298 K (Fig. S32d†). On the other hand, JNU-6-CF_3 was synthesized by using 5-trifluoromethyl-4-carboxylic acid as a ligand. JNU-6-CF_3 also shows preferential adsorption of C_2H_6 over C_2H_4. The maximum uptake of C_2H_6 on JNU-6-CF_3 is 3.49 mmol g^{-1} (Fig. S34b†), which is nearly 25% less than that of JNU-6-CH_3, likely due to the reduced porosity of JNU-6-CF_3 (Fig. S35a†). The water vapor adsorption isotherm of JNU-6-CF_3 displays almost no water uptake over the entire pressure range (Fig. S34c†), reflecting its extremely high hydrophobicity. We evaluated dynamic column breakthrough experiments on JNU-6-CF_3 for a C_2H_6/C_2H_4 (50/50, v/v) mixture at a flow rate of 2.0 mL min^{-1} and 298 K. As shown in Fig. S34d,† a clean separation of C_2H_6 from the C_2H_6/C_2H_4 mixture can be realized under either dry or 98% RH conditions with no obvious decrease in separation performance. Based on the breakthrough curves, *ca.* 10.5 L kg^{-1} of high-purity C_2H_4 ($\geq$99.95%) can be recovered from the C_2H_4/C_2H_6 (50/50) mixture in a single breakthrough operation, which is about half of that of JNU-6-CH_3. The results indicate that further increase of methylation degree or introducing more hydrophobic CF_3 groups may not be necessarily favorable for the C_2H_6/C_2H_4 separation, and both adsorption capacity and adsorption selectivity have to be considered to achieve high separation efficiency.

In summary, we have successfully demonstrated a surface engineering strategy to boost the separation potential of C_2H_4 from C_2H_6/C_2H_4 mixtures under either dry or humid conditions. The introduction of CH_3 groups on an isoreticular MOF-5 analogue (JNU-6) renders the obtained JNU-6-CH_3 with enhanced hydrolytic stability and a more suitable pore environment for C_2H_6/C_2H_4 separation. JNU-6-CH_3 retains its framework integrity even after being immersed in water for six months, and it exhibits large C_2H_6 adsorption capacity (4.63 mmol g^{-1}) and high C_2H_6/C_2H_4 adsorption selectivity (1.67) due to the optimized pore size and surface function. Breakthrough experiments reveal benchmark productivity of 22.06 and 18.71 L kg^{-1} of high-purity C_2H_4 ($\geq$99.95%) from a C_2H_6/C_2H_4 (50/50, v/v) mixture under dry and humid conditions, respectively. This work offers a promising approach for designing MOFs to overcome the adsorption/selectivity trade-off limitation in paraffin/olefin separation.

Data availability

The data that support the plots within this paper and other findings of this study are available from the corresponding authors upon reasonable request. The X-ray crystallographic coordinates for structures reported in this Article have been deposited at the Cambridge Crystallographic Data Centre (CCDC), under deposition numbers CCDC 2259108, 2258075, and 2286047.†https://www.ccdc.cam.ac.uk/data_request/cif

Author contributions

H. Z., W. L., and D. L. conceived and designed the research. X.-J. X., H. Z., and W. L. co-wrote the manuscript. X.-J. X. and Q.-Y. C. planned and executed the synthesis, characterization, and gas separation studies. Y. W. and R. H. performed the theoretical simulations. X.-J. X. carried out the structural analyses. All authors participated in and contributed to the preparation of the manuscript.

Conflicts of interest

There are no conflicts to declare.

Acknowledgements

This work was financially supported by the National Natural Science Foundation of China (21731002, 21975104, 22150004, 22271120, and 22301102), the Ministry of Science and Technology of China (2021ZD0303102), the Guangdong Basic and Applied Basic Research Foundation (2023A1515010952), the Innovation Team Project in Guangdong Colleges and Universities (2021KCXTD009), and the National Postdoctoral Program for Innovative Talent (BX20220132).

Notes and references

1 D. S. Sholl and R. P. Lively, *Nature*, 2016, **532**, 435–437.
2 https://www.fortunebusinessinsights.com/ethylene-market-104532.
3 S. Chu, Y. Cui and N. Liu, *Nat. Mater.*, 2017, **16**, 16–22.
4 H. Zeng, M. Xie, T. Wang, R.-J. Wei, X.-J. Xie, Y. Zhao, W. Lu and D. Li, *Nature*, 2021, **595**, 542–548.
5 X. W. Gu, J. X. Wang, E. Wu, H. Wu, W. Zhou, G. Qian, B. Chen and B. Li, *J. Am. Chem. Soc.*, 2022, **144**, 2614–2623.
6 S. Furukawa, J. Reboul, S. Diring, K. Sumida and S. Kitagawa, *Chem. Soc. Rev.*, 2014, **43**, 5700–5734.
7 H. Furukawa, K. E. Cordova, M. O'Keeffe and O. M. Yaghi, *Science*, 2013, **341**, 1230444.
8 Z. Chen, K. O. Kirlikovali, P. Li and O. K. Farha, *Acc. Chem. Res.*, 2022, **55**, 579–591.
9 R. B. Lin, L. Li, H. L. Zhou, H. Wu, C. He, S. Li, R. Krishna, J. Li, W. Zhou and B. Chen, *Nat. Mater.*, 2018, **17**, 1128–1133.
10 Y. P. Li, Y. N. Zhao, S. N. Li, D. Q. Yuan, Y. C. Jiang, X. Bu, M. C. Hu and Q. G. Zhai, *Adv. Sci.*, 2021, **8**, 2003141.
11 A. A. Lysova, D. G. Samsonenko, K. A. Kovalenko, A. S. Nizovtsev, D. N. Dybtsev and V. P. Fedin, *Angew. Chem., Int. Ed.*, 2020, **59**, 20561–20567.
12 Q. Liao, W. X. Zhang, J. P. Zhang and X. M. Chen, *Nat. Commun.*, 2015, **6**, 8697–8705.
13 H. Zeng, X. J. Xie, M. Xie, Y. L. Huang, D. Luo, T. Wang, Y. Zhao, W. Lu and D. Li, *J. Am. Chem. Soc.*, 2019, **141**, 20390–20398.
14 H. G. Hao, Y. F. Zhao, D. M. Chen, J. M. Yu, K. Tan, S. Q. Ma, Y. Chabal, Z. M. Zhang, J. M. Dou, Z. H. Xiao, G. Day, H. C. Zhou and T. B. Lu, *Angew. Chem., Int. Ed.*, 2018, **57**, 16067–16071.
15 G. D. Wang, Y. Z. Li, W. J. Shi, L. Hou, Y. Yu. Wang and Z. H. Zhu, *Angew. Chem., Int. Ed.*, 2022, **61**, e202205427.
16 J. W. Cao, S. Mukherjee, T. Pham, Y. Wang, T. Wang, T. Zhang, X. Jiang, H. J. Tang, K. A. Forrest, B. Space, M. J. Zaworotko and K.-J. Chen, *Nat. Commun.*, 2021, **12**, 6507.

17 L. Li, R. B. Lin, R. Krishna, H. Li, S. Xiang, H. Wu, J. Li, W. Zhou and B. Chen, *Science*, 2018, **362**, 443–446.

18 Z. Di, C. Liu, J. Pang, S. Zhou, Z. Ji, F. Hu, C. Chen, D. Yuan, M. Hong and M. Wu, *Angew. Chem., Int. Ed.*, 2022, **134**, e202210343.

19 C. X. Chen, Z. W. Wei, J. J. Jiang, S.-P. Zheng, H.-P. Wang, Q.-F. Qiu, C.-C. Cao, D. Fenske and C.-Y. Su, *J. Am. Chem. Soc.*, 2017, **139**, 6034–6037.

20 Z. Di, C. Liu, J. Pang, C. Chen, F. Hu, D. Yuan, M. Wu and M. Hong, *Angew. Chem., Int. Ed.*, 2021, **60**, 10828–10832.

21 S. Xing, J. Liang, P. Brandt, F. Schäfer, A. Nuhnen, T. Heinen, I. Boldog, J. Möllmer, M. Lange, O. Weingart and C. Janiak, *Angew. Chem., Int. Ed.*, 2021, **60**, 17998–18005.

22 C. Montoro, F. Linares, E. Quartapelle Procopio, I. Senkovska, S. Kaskel, S. Galli, N. Masciocchi, E. Barea and J. A. R. Navarro, *J. Am. Chem. Soc.*, 2011, **133**, 11888–11891.

23 B. Tu, Q. Pang, D. Wu, Y. Song, L. Weng and Q. Li, *J. Am. Chem. Soc.*, 2014, **136**, 14465–14471.

24 C. Feng, H. Zhao and Z.-Q. Li, *J. Solid State Chem.*, 2018, **258**, 841–844.

25 L. Wang, W. Xue, H. Zhu, X. Guo, H. Huang and C. Zhong, *Angew. Chem., Int. Ed.*, 2023, **135**, e202218596.

26 Z. Zhang, S. B. Peh, Y. Wang, Y. Wang, C. Kang, W. Fan and D. Zhao, *Angew. Chem., Int. Ed.*, 2020, **132**, 19089–19094.

27 R. B. Lin, H. Wu, L. Li, X. L. Tang, Z. Li, J. Gao, H. Cui, W. Zhou and B. L. Chen, *J. Am. Chem. Soc.*, 2018, **140**, 12940–12946.

28 O. T. Qazvini, R. Babarao, Z.-L. Shi, Y.-B. Zhang and S. G. Telfer, *J. Am. Chem. Soc.*, 2019, **141**, 5014–5020.

29 S. B. Geng, E. Lin and X. Li, *J. Am. Chem. Soc.*, 2021, **143**, 8654–8660.

30 M. Kang, S. Yoon, S. Ga, D. W. Kang, S. Han, J. H. Choe, H. Kim, D. W. Kim, Y. G. Chung and C. S. Hong, *Adv. Sci.*, 2021, **8**, 2004940.

31 Z. Xu, X. Xiong, J. Xiong, R. Krishna, L. Li, Y. Fan, F. Luo and B. Chen, *Nat. Commun.*, 2020, **11**, 3163.

32 B. Zhu, J. Cao, S. Mukherjee, T. Pham, T. Zhang, T. Wang, X. Jiang, K. A. Forrest and M. J. Zaworotko, *J. Am. Chem. Soc.*, 2021, **143**, 1485–1492.

33 J. Pires, M. L. Pinto and V. K. Saini, *ACS Appl. Mater. Interfaces*, 2014, **6**, 12093–12099.

34 S. Meng, H. Ma, L. Jiang, H. Ren and G. Zhu, *J. Mater. Chem. A*, 2014, **2**, 14536–14541.

35 K. J. Chen, D. G. Madden, S. Mukherjee, T. Pham, K. A. Forrest, A. Kumar, B. Space, J. Kong, Q. Y. Zhang and M. J. Zaworotko, *Science*, 2019, **366**, 241–246.

36 D. Dubbeldam, S. Calero, D. E. Ellis and R. Q. Snurr, *Mol. Simul.*, 2016, **42**, 81–101.

37 G. D. Wang, R. Krishna, Y. Z. Li, W. J. Shi, L. Hou, Y. Y. Wang and Z. H. Zhu, *Angew. Chem., Int. Ed.*, 2022, **61**, e202213015.

38 H.-G. Hao, Y.-F. Zhao, D.-M. Chen, J.-M. Yu, K. Tan, S. Ma, Y. Chabal, Z.-M. Zhang, J.-M. Dou, Z.-H. Xiao, G. Day, H.-C. Zhou and T.-B. Lu, *Angew. Chem., Int. Ed.*, 2018, **130**, 16299–16303.

Supporting Information

Surface Engineering on a Microporous Metal-Organic Framework to Boost Ethane/Ethylene Separation under Humid Conditions

Xiao-Jing Xie,[a] Ying Wang,[a] Qi-Yun Cao,[a] Rajamani Krishna,[b] Heng Zeng,*[a] Weigang Lu,*[a] Dan Li[a]

[a]College of Chemistry and Materials Science, Guangdong Provincial Key Laboratory of Functional Supramolecular Coordination Materials and Applications, Jinan University, Guangzhou 510632, P. R. China.

[b]Van't Hoff Institute for Molecular Sciences, University of Amsterdam, Science Park 904, Amsterdam 1098 XH, Netherlands.

*Corresponding author. Email: zengheng90@163.com; weiganglu@jnu.edu.cn;

Materials and synthesis methods

Materials

All reagents and materials were commercially available and used as received without further purification.

Syntheses of JNU-6

A mixture of pyrazole-4-carboxylic acid (300 mg, 2.68 mmol), $Zn(NO_3)_2 \cdot 6H_2O$ (7140 mg, 24 mmol), and N,N-Diethylformamide (DEF, 120 mL) was placed in a 350 mL of glass vial and heated at 100 °C for 12 h. After cooling down to room temperature, the block crystals were washed with methanol 10 times at 25 °C and then dried under high vacuum at 90 °C.

Syntheses of JNU-6-CH_3 and JNU-6-$(CH_3)_2$

A mixture of 3-methylpyrazole-4-carboxylic acid (378 mg, 3.25 mmol), $Zn(NO_3)_2 \cdot 6H_2O$ (900 mg, 3.02 mmol), N,N-Diethylformamide (DEF, 120 mL), deionized water (30 mL), and nitric acid (0.1 mol/L, 4.5 mL) was placed in a 350 mL of glass vial and heated at 120 °C for 12 h. After cooling down to room temperature, the block crystals were washed with methanol 10 times at 70 °C and then dried under high vacuum at 200 °C. The syntheses of JNU-6-$(CH_3)_2$ is consistent with that of JNU-6-CH_3.

Syntheses of JNU-6-CF_3

A mixture of 5-trifluoromethyl-4-carboxylic acid (560 mg, 4.0 mmol), $Zn(NO_3)_2 \cdot 6H_2O$ (1200 mg, 4.02 mmol), *N*,*N*-Dimethylformamide (DMF, 90 mL), ethanol (30 mL) was placed in a 350 mL of glass vial and heated at 120 °C for 12 h. After cooling down to room temperature, the block crystals were washed with methanol 10 times at 70 °C and then dried under high vacuum at 200 °C.

Gas adsorption measurement

At least 100 mg of sample were activated under dynamic vacuum (below 5 μmHg) for 24 h. Single-component gas adsorption isotherms were obtained on an ASAP 2020 PLUS Analyzer (Micromeritics).

Powder X-ray diffraction (PXRD) analysis

Powder X-ray diffraction data were recorded with microcrystalline samples on a Rigaku Ultima IV diffractometer (40 kV, 40 mA, Cu Kα, λ = 1.5418 Å). The measurement parameters include a scan speed of 10°/min, a step size of 0.02°, and a scan range of 2θ from 5° to 30°. For variable temperature PXRD measurements, the measurement parameters include a scan speed of 2°/min, a step size of 0.02°, and a scan range of 2θ from 5° to 30°.

Thermogravimetric analysis (TGA)

About 5 mg of dried samples was used on a Q50 thermogravimetric analyzer (TGA) from 40 to 800 °C under a N_2 flow with a heating rate of 10 °C/min.

The isosteric enthalpy of adsorption (Q_{st})

The unary isotherm data for C_2H_6 and C_2H_4, measured at three different temperatures 273 K, 283 K, and 298 K in JNU-6 and JNU-6-CH_3 were fitted with excellent accuracy using the dual-site Langmuir-Freundlich model, where we distinguish two distinct adsorption sites A and B:

$$q = q_{sat,A}\frac{b_A p^{vA}}{1+b_A p^{vA}} + q_{sat,B}\frac{b_B p^{vB}}{1+b_B p^{vB}} \qquad \text{(S1)}$$

In eq S1, the Langmuir-Freundlich parameters b_A and b_B are both temperature dependent

$$b_A = b_{A0}\exp\left(\frac{E_A}{RT}\right);\ b_B = b_{B0}\exp\left(\frac{E_B}{RT}\right) \qquad \text{(S2)}$$

In eq S2, E_A, E_B are the energy parameters associated with sites A, and B, respectively.

The fit parameters are provided in Table S2, and Table S3.

The isosteric heat of adsorption, Q_{st}, is defined as

$$Q_{st} = -RT^2\left(\frac{\partial \ln p}{\partial T}\right)_q \qquad \text{(S3)}$$

where the derivative in the right member of eq S3 is determined at constant adsorbate loading, q. The derivative was determined by analytic differentiation of the combination of eq S1, eq S2, and eq S3.

IAST selectivities and separation potential

A key metric that quantifies the efficacy of a MOF for separation of binary $C_2H_6(1)/C_2H_4(2)$ mixtures is the adsorption selectivity, S_{ads}, defined by

$$S_{ads} = \frac{q_1/q_2}{p_1/p_2} \quad \text{(S1)}$$

where q_1 and q_2 are the molar loadings of the guest components in the adsorbed phase in equilibrium with a bulk gas phase mixture with partial pressures p_1 and p_2. The mixture adsorption equilibrium is commonly determined using the Ideal Adsorbed Solution theory (IAST)[1] using fits of unary isotherms as input data.

These mixture separations are envisaged to be carried out in fixed bed adsorbers. In such devices, the separations are dictated by a combination of adsorption selectivity and uptake capacity. Using the shock wave model for fixed bed adsorbers, Krishna[2, 3] has suggested that the appropriate metric is the separation potential, Δq_1.

$$\Delta q = q_1 \frac{y_{20}}{y_{10}} - q_2 \quad \text{(S5)}$$

In eq S5 y_{10}, y_{20} are the mole fractions of the feed mixture during the adsorption cycle. In the derivation of eq S5, it is assumed that the concentration "fronts" traversed the column in the form of shock waves during the desorption cycle. The molar loadings q_1, q_2 of the two components are determined using the Ideal Adsorbed Solution Theory (IAST) of Myers and Prausnitz using the unary isotherm fits as data inputs.[1] The physical significance of Δq is the maximum productivity of pure C_2H_4 (2) that is achievable in the adsorption cycle of PSA operations.

The IAST calculations of S_{ads}, and Δq were performed for binary 50/50 C_2H_6(1)/C_2H_4 (2) mixtures at 298 K, at total pressures ranging from 1 to 100 kPa.

Computational details

Grand Canonical Monte Carlo (GCMC) simulations were performed to simulate the single-component adsorption of C_2H_6 and C_2H_4 on JNU-6 and JNU-6-CH_3 by RASPA2 software.[2,3] These frameworks were considered to be rigid, and the optimized gas molecules were used. The interaction energies between the gas molecules and framework were computed through the Coulomb and Lennard-Jones 6-12 (LJ) potentials. The simulation box of the GCMC run was constructed by 2×2×2 supercell of the respective MOFs, and the cut-off radius was chosen as 14 Å. The Lennard–Jones (LJ) parameters for frameworks were taken from Dreiding force field[4], and if not available, from the universal force field (UFF).[5] The LJ parameters for gas molecules were taken from literature.[6,7] The LJ parameters of different atom types were computed using the Lorentz-Berthelot mixing rules. The long-range electrostatic interactions were calculated by using Ewald summation. The equilibration steps and production steps were both set as 1.0×10^7. The DDEC charges[8] calculated by the

Vienna ab initio simulation package (VASP)[9,10], were employed to the framework atoms. Perdew-Burke-Ernzerhof (PBE) functional with generalized gradient approximation (GGA) was used to evaluate the electron exchange correlation.

To further quantify the binding energies between framework and gas molecules, dispersion-corrected density functional theory (DFT-D) calculations were performed based on the cluster models extracted from the structures of JNU-6 and JNU-6-CH_3. The truncated bonds of the cluster models were saturated with hydrogen atoms or methyl groups. All geometry optimizations were performed at the B3LYP-D3(BJ)/6-31G* level for the non-metal atoms.[11-13] For Zn atom, the LanL2DZ basis set[14] was used to consider the relativistic effects. Frequency analyses were performed at the same computational level to confirm local minima for each optimized structure. Based on the optimized geometries, these binding energies (ΔE) were corrected from the basis set superposition error (BSSE) by the counterpoise procedure.[15] All these DFT-D calculations were accomplished using Gaussian 16 software.[16] The binding energy (ΔE) was calculated by the following equation:

$$\Delta E = E_{gas+MOF} - E_{MOF} - E_{gas} + E_{BSSE}$$

Where $E_{gas+MOF}$, E_{MOF}, E_{gas} are the optimization energy of MOF with an adsorbed gas molecule, MOF structure and isolated gas molecule, respectively. while the E_{BSSE} can correct for weak intermolecular interactions.

To reveal the nature of the intermolecular interaction vividly, the electrostatic potential (ESP) on van der Waals (vdW) surface[17,18] and the independent gradient model based on Hirshfeld partition (IGMH) analyses[19] were performed. The ESP and IGMH analyses were achieved by Multiwfn 3.8 program[20] based on the wave function files generated by DFT-D calculations. Molecular graphs of ESP and IGMH maps were rendered by means of Visual Molecular Dynamics (VMD) 1.9.3 software.[21]

Column breakthrough experiments:

The breakthrough experiments were carried out under ambient conditions (298 K, 1 bar) by using a lab-scale fixed-bed system (Figs. S36 and S37). The activated sample JNU-6 (1.01 g) , JNU-6-CH_3 (0.85 g), JNU-6-$(CH_3)_2$ (0.92 g), and JNU-6-CF_3 (0.9 g) were packed into a custom-made stainless-steel column (3.15 mm ID × 450 mm) and then was activated under high vacuum for 12 h.

For C_2H_6/C_2H_4 and $C_2H_2/C_2H_6/C_2H_4$, the gas mixture of C_2H_6/C_2H_4 (1/1, v/v) or $C_2H_6/C_2H_4/C_2H_2$ (1/1/1, v/v/v) was introduced into breakthrough apparatus with a total flow rate of 2.0 mL·min^{-1}. The outlet effluent of the column was continuously monitored using a gas chromatograph (GC-7890B, Agilent) with a thermal conductivity detector (TCD).

For $C_2H_6/C_2H_4/CO_2$, the gas mixture of $C_2H_6/C_2H_4/CO_2$ (1/1/1, v/v/v) was introduced into breakthrough apparatus with a total flow rate of 2.0 mL·min^{-1}. The outlet effluent of the column was continuously monitored using a gas chromatograph (GC-7890B, Agilent) with a thermal conductivity detector (TCD).

The sample was regenerated *in-situ* in the column at 298 K with helium sweeping for 12 h in the cyclic test. The complete breakthrough of C_2H_6 was indicated by the downstream gas composition reaching that of the feed gas. On the basis of the mass balance, the gas adsorption capacities can be determined as follows[22]:

$$q_i = \frac{C_i V}{22.4 \times m} \times \int_0^t \left(1 - \frac{F}{F_0}\right) dt$$

Where q_i is the equilibrium adsorption capacity of gas i (mmol/g), C_i is the feed gas concentration, V is the volumetric feed flow rate (mL/min), t is the adsorption time (min), F_0 and F are the inlet and outlet gas molar flow rates, respectively, and m is the mass of the adsorbent (g).

The C_2H_6 purity (c) is defined by the peak area of C_2H_6, we calculated C_2H_6 purity according to the following equation:

$$\mathrm{c} = \frac{C_i(\mathrm{C_2H_6})}{C_i(\mathrm{C_2H_6}) + C_i(\mathrm{C_2H_4})}$$

where C_i (C_2H_6) and C_i (C_2H_4) represent the peak areas of component C_2H_6 and C_2H_4 in a single injection.

Transient breakthrough simulations

Transient breakthrough simulations were carried out for binary C_2H_6/C_2H_4 (50/50) feed mixture at 298 K and 100 kPa total pressure using JNU-6-CH_3. The simulation methodology is described in earlier publications.[23-27] In these simulations, the intra-crystalline diffusional influences are considered to be of negligible importance.

The bed dimensions and operating conditions are the same as in the experiments: length of packed bed, L = 450 mm; inside tube diameter = 3.15 mm; volumetric flow rate of gas mixture at the entrance to the bed, $Q_0 = 2$ mL min^{-1}; mass of JNU-6-CH_3 in packed tube = 0.85 g.

Table S1 Comparison of molecular sizes and physical properties of C_2H_4 and C_2H_6.[28]

Molecule	**Boiling point (°C)**	**Polarizability (×10^{-25} cm^3)**	**Kinetic diameter (Å)**	**Molecular size (Å^3)**
C_2H_4	169.4	42.52	4.163	3.28 × 4.18 × 4.84
C_2H_6	184.5	44.3 – 44.7	4.443	4.08 × 3.81 × 4.82

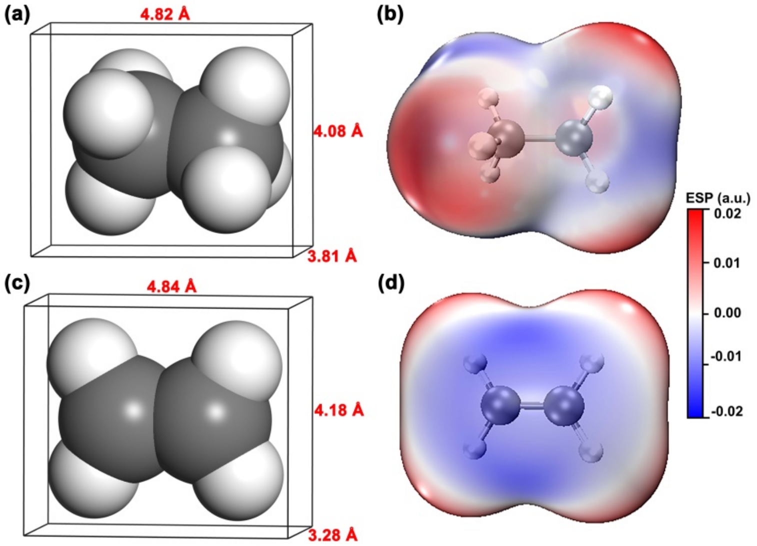

Fig. S1 (a) Molecular size and (b) electrostatic potential of C_2H_6. (c) Molecular size and (d) electrostatic potential of C_2H_4. Electrostatic potential (ESP) analysis was performed by the Multiwfn software package.[29,30]

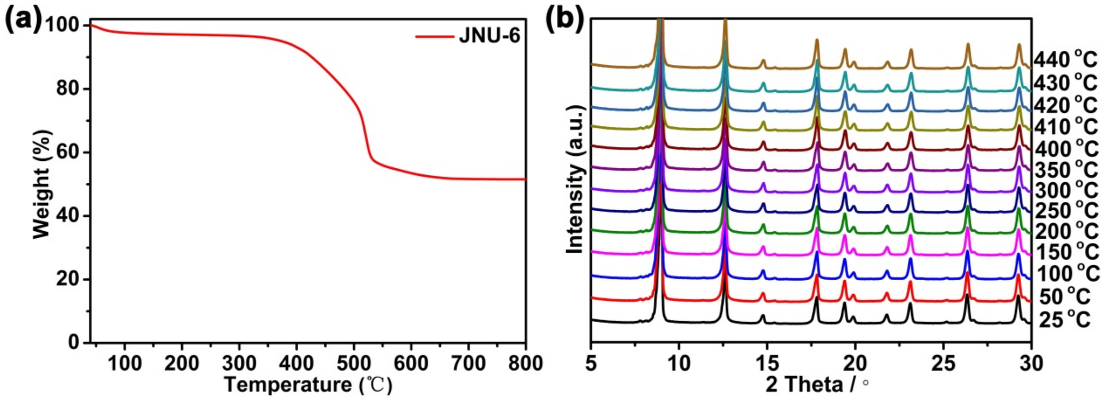

Fig. S2 (a) Thermogravimetric analysis (TGA) curves of the activated JNU-6. (b) *In-situ* variable-temperature PXRD (VT-PXRD) patterns of JNU-6 under the N_2 atmosphere.

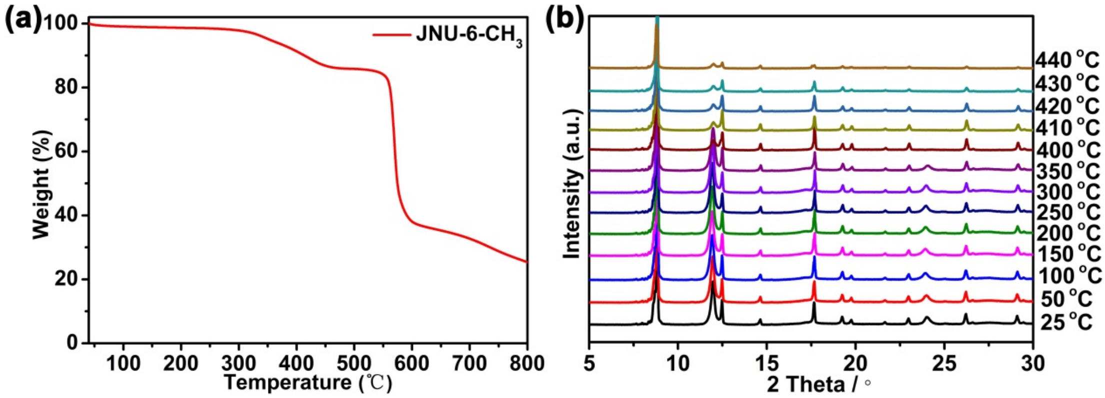

Fig. S3 (a) Thermogravimetric analysis (TGA) curves of the activated JNU-6-CH_3. (b) *In-situ* variable-temperature PXRD (VT-PXRD) patterns of JNU-6-CH_3 under the N_2 atmosphere.

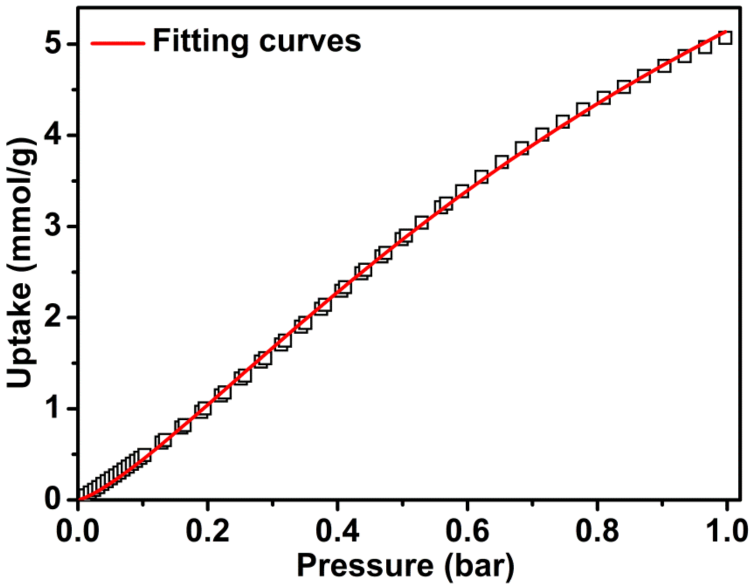

Fig. S4 Dual-site Langmuir-Freundlich fitting for the C_2H_6 adsorption isotherm of JNU-6 at 298 K.

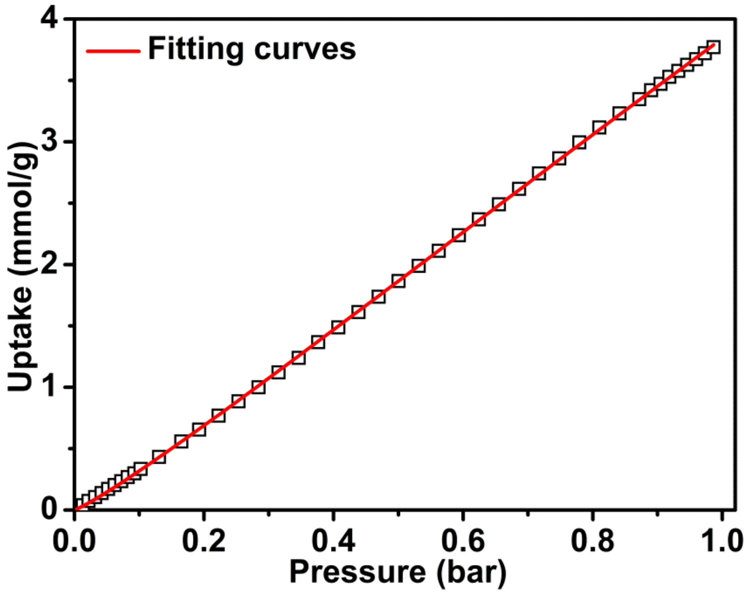

Fig. S5 Dual-site Langmuir-Freundlich fit for the C_2H_4 adsorption isotherm of JNU-6 at 298 K.

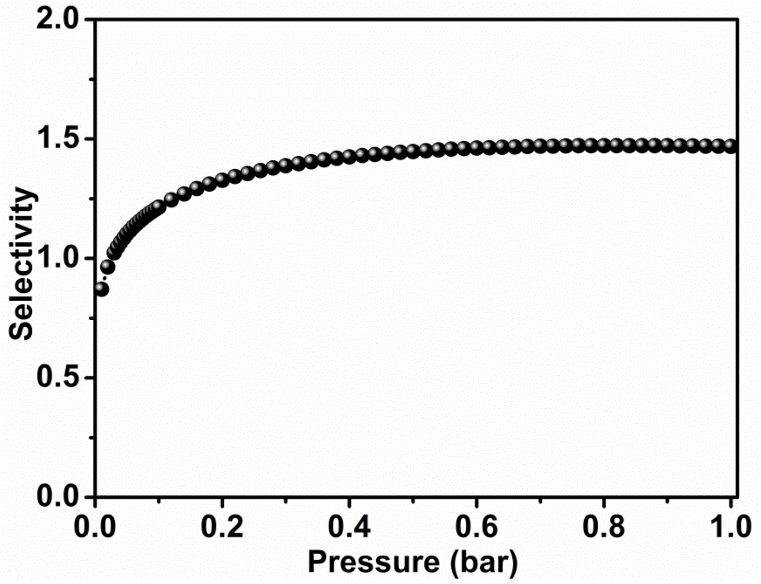

Fig. S6 IAST selectivity of JNU-6 for an equimolar C_2H_6/ C_2H_4 mixture at 298 K.

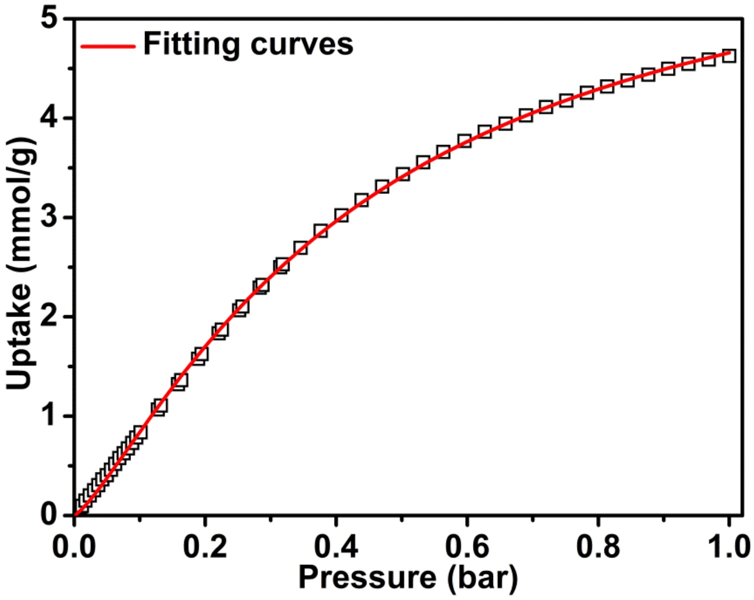

Fig. S7 Dual-site Langmuir-Freundlich fitting for the C_2H_6 adsorption isotherm of JNU-6-CH_3 at 298 K.

Fig. S8 Dual-site Langmuir-Freundlich fitting for the C_2H_4 adsorption isotherm of JNU-6-CH_3 at 298 K.

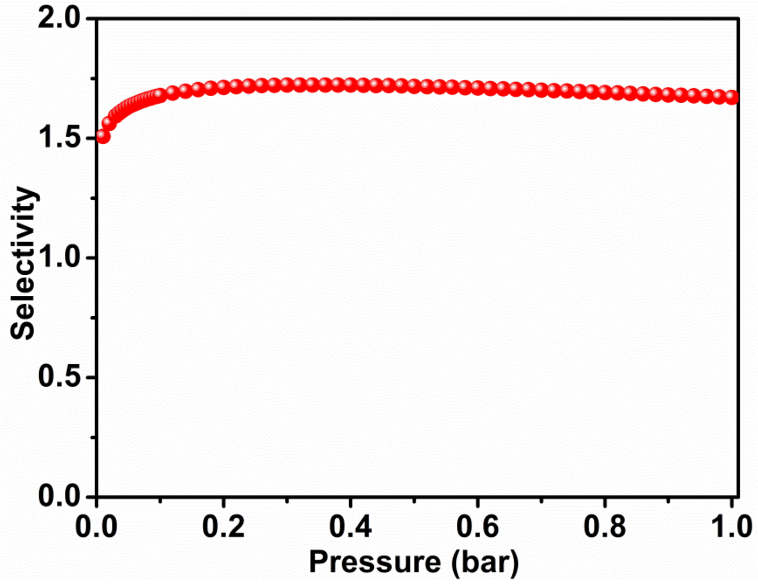

Fig. S9 IAST selectivity of JNU-6-CH_3 for an equimolar C_2H_6/C_2H_4 mixture at 298 K.

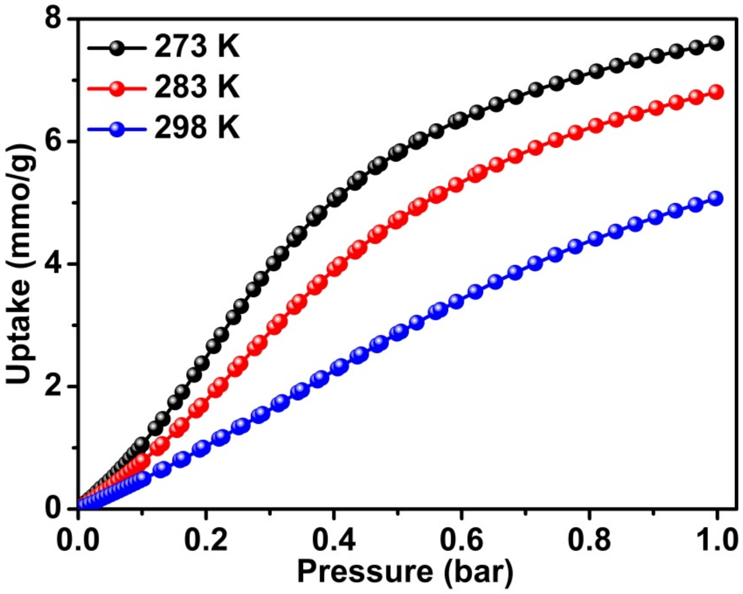

Fig. S10 C_2H_6 adsorption isotherms of JNU-6 at 273, 283, and 298 K.

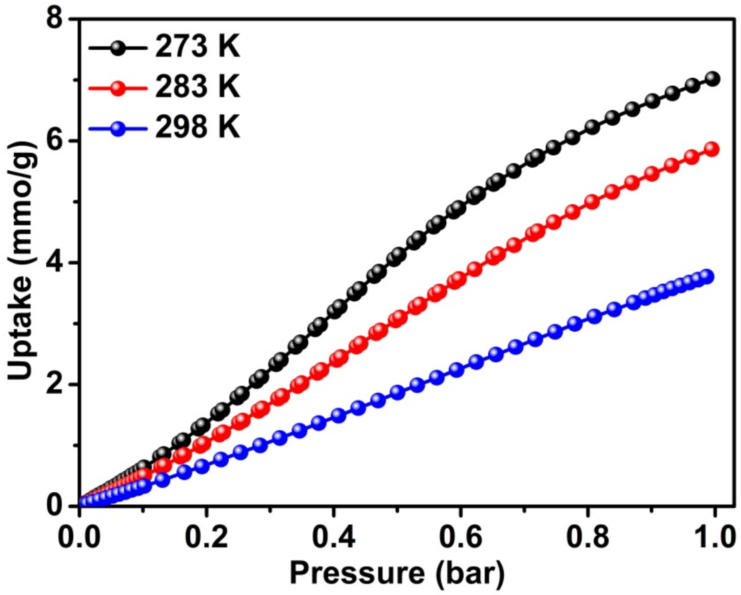

Fig. S11 C_2H_4 adsorption isotherms of JNU-6 at 273, 283, and 298 K.

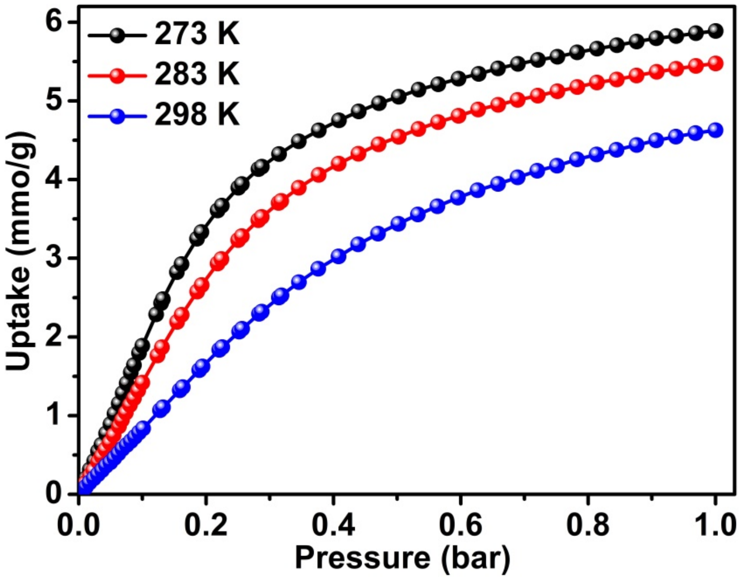

Fig. S12 C_2H_6 adsorption isotherms of JNU-6-CH_3 at 273, 283, and 298 K.

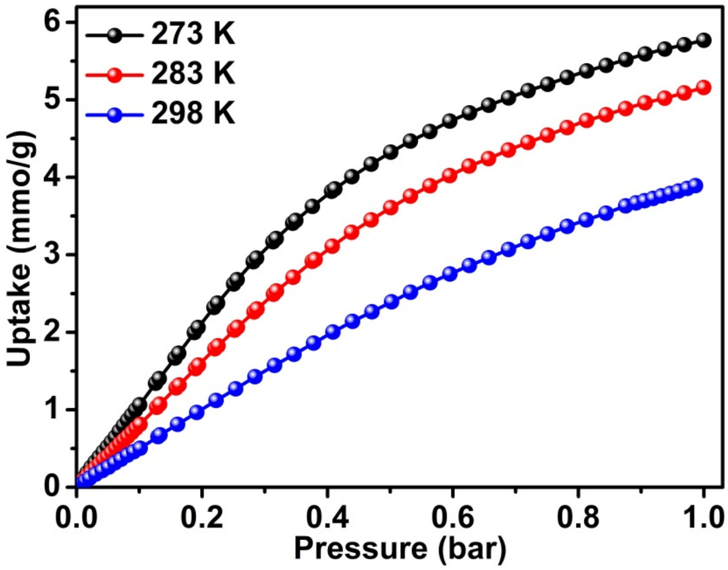

Fig. S13 C_2H_4 adsorption isotherms of JNU-6-CH_3 at 273, 283, and 298 K.

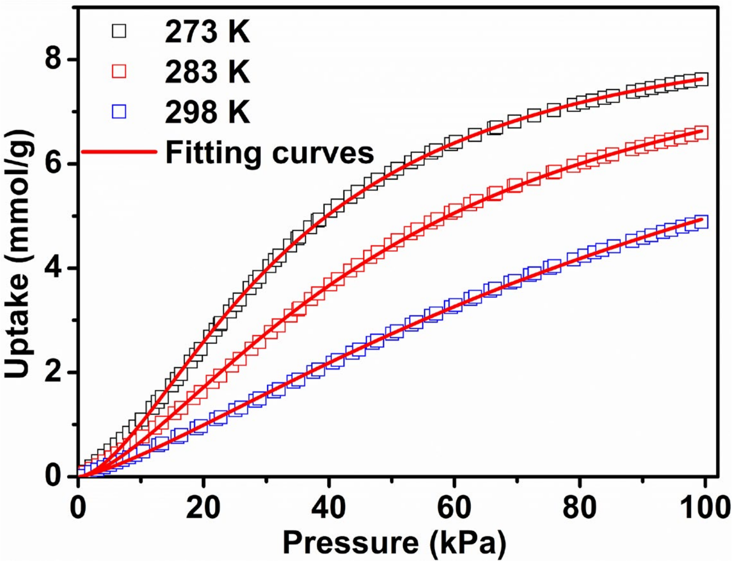

Fig. S14 Dual-site Langmuir-Freundlich fitting of the C_2H_6 adsorption isotherms of JNU-6 at 273, 283, and 298 K.

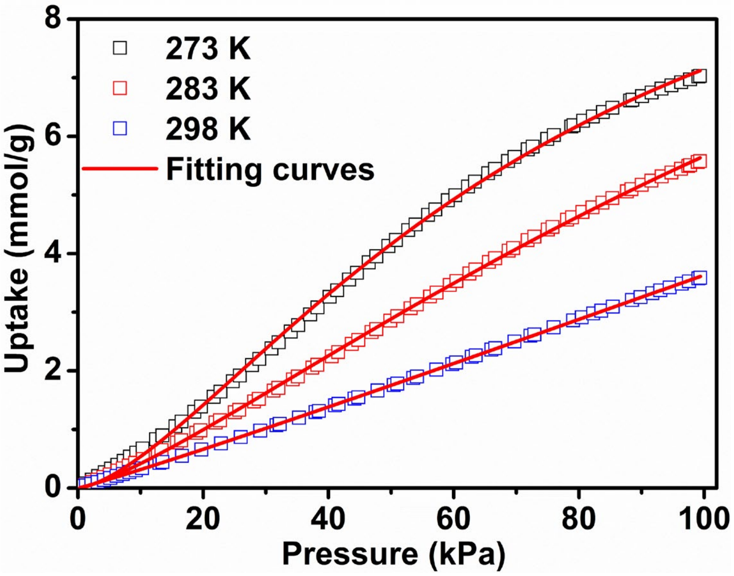

Fig. S15 Dual-site Langmuir-Freundlich fitting of the C_2H_4 adsorption isotherms of JNU-6 at 273, 283, and 298 K.

Table 2. Dual-site Langmuir-Freundlich fits for C_2H_6 and C_2H_4 in JNU-6.

	Site A				Site B			
	$\frac{q_{A,sat}}{\text{mol kg}^{-1}}$	$\frac{b_{A,0}}{\text{Pa}^{-v_A}}$	$\frac{E_A}{\text{kJ mol}^{-1}}$	v_A	$\frac{q_{B,sat}}{\text{mol kg}^{-1}}$	$\frac{b_{B,0}}{\text{Pa}^{-v_B}}$	$\frac{E_B}{\text{kJ mol}^{-1}}$	v_B
C_2H_6	2.55	1.067E-16	15.9	0.88	11.2	1.930E-12	30.3	1.26
C_2H_4	2.55	1.067E-16	16	1	41	3.840E-11	22.7	1.085

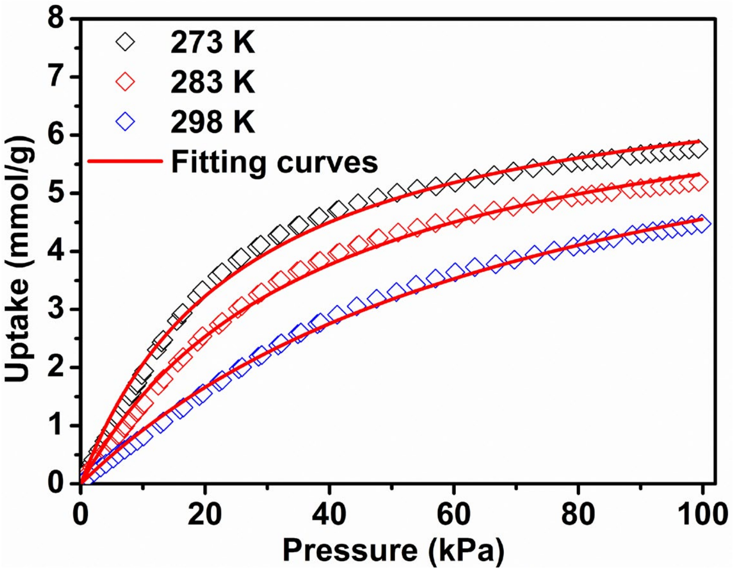

Fig. S16 Dual-site Langmuir-Freundlich fitting of the C_2H_6 adsorption isotherms of JNU-6-CH_3 at 273, 283, and 298 K.

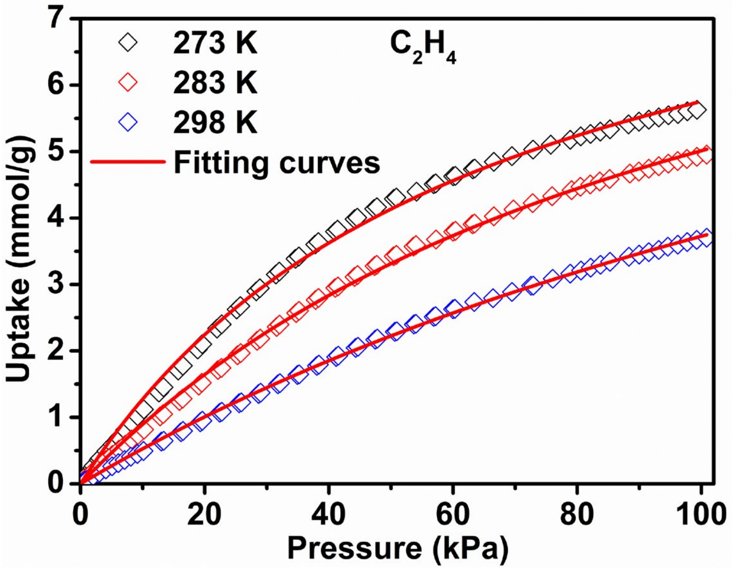

Fig. S17 Dual-site Langmuir-Freundlich fitting of the C_2H_4 adsorption isotherms of JNU-6-CH_3 at 273, 283, and 298 K.

Table S3. Dual-site Langmuir-Freundlich fits for C_2H_6, and C_2H_4 in JNU-6-CH_3.

	Site A				Site B			
	$\frac{q_{A,sat}}{\text{mol kg}^{-1}}$	$\frac{b_{A,0}}{\text{Pa}^{-\nu_A}}$	$\frac{E_A}{\text{kJ mol}^{-1}}$	ν_A	$\frac{q_{B,sat}}{\text{mol kg}^{-1}}$	$\frac{b_{B,0}}{\text{Pa}^{-\nu_B}}$	$\frac{E_B}{\text{kJ mol}^{-1}}$	ν_B
C_2H_6	2.55	1.067E-16	16	1	7.1	1.671E-10	26.5	1.075
C_2H_4	2.55	1.067E-16	16	1	9.7	2.574E-10	24.4	1.02

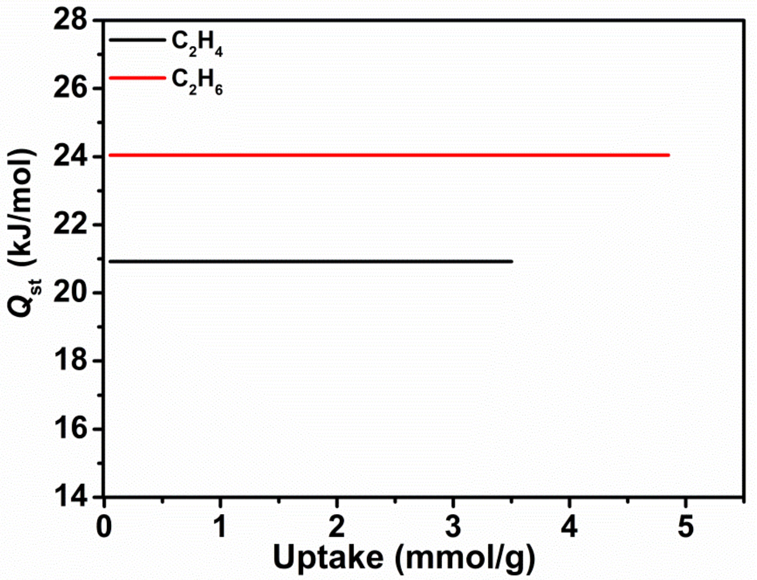

Fig. S18 Calculated C_2H_6 and C_2H_4 adsorption enthalpy (Q_{st}) of JNU-6.

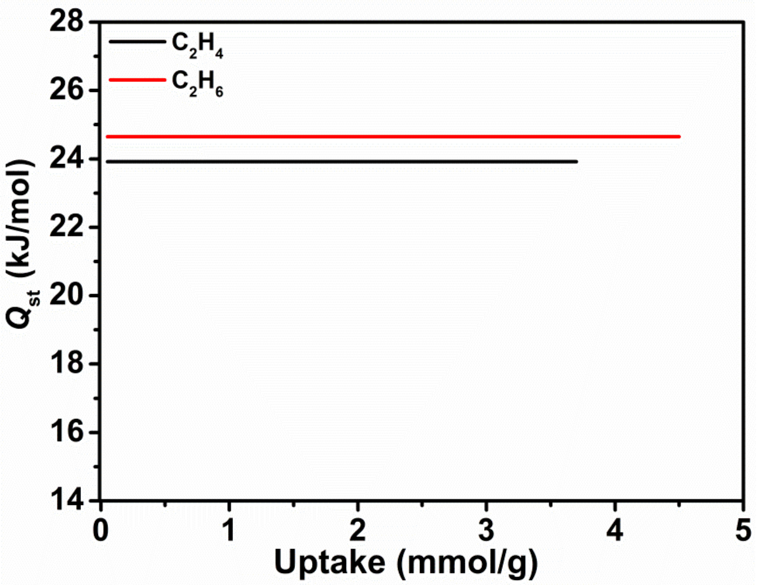

Fig. S19 Calculated C_2H_6 and C_2H_4 adsorption enthalpy (Q_{st}) of JNU-6-CH_3.

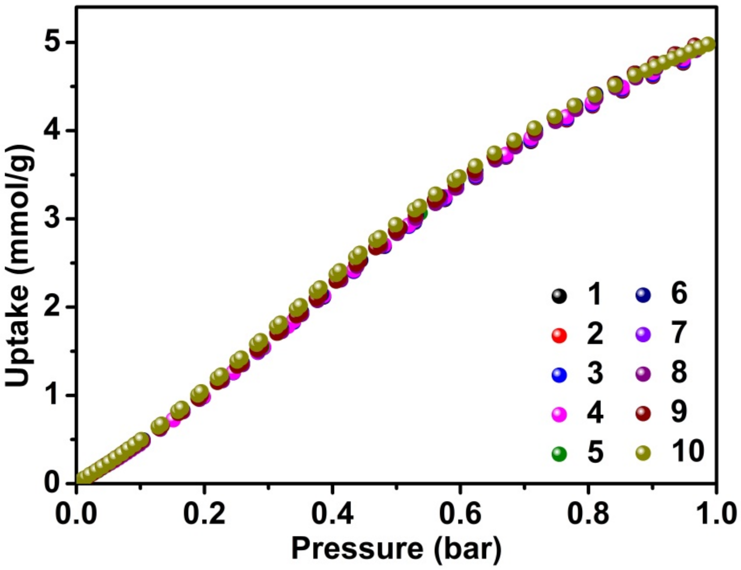

Fig. S20 Continuous C_2H_6 adsorption measurements on JNU-6 at 298 K.

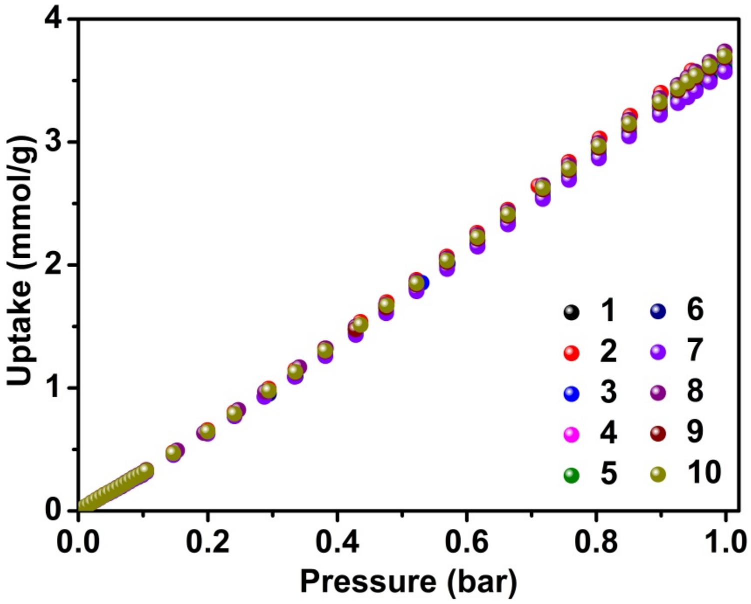

Fig. S21 Continuous C_2H_4 adsorption measurements on JNU-6 at 298 K.

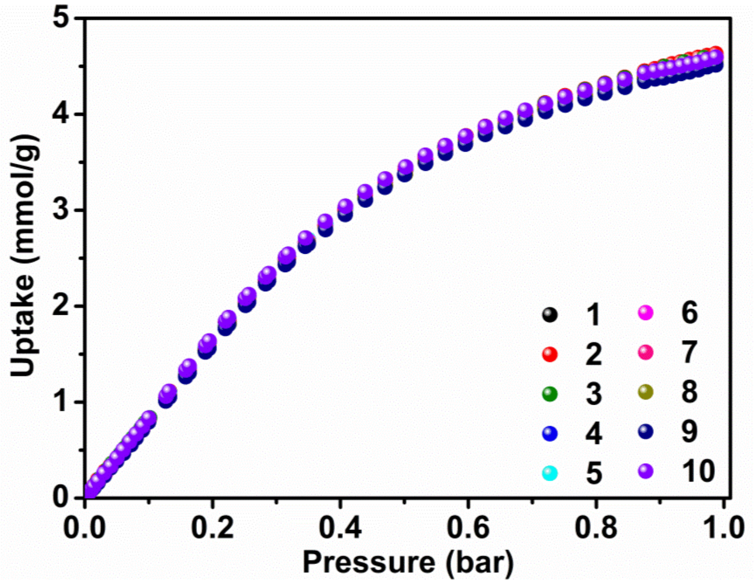

Fig. S22 Continuous C_2H_6 adsorption measurements on JNU-6-CH_3 at 298 K.

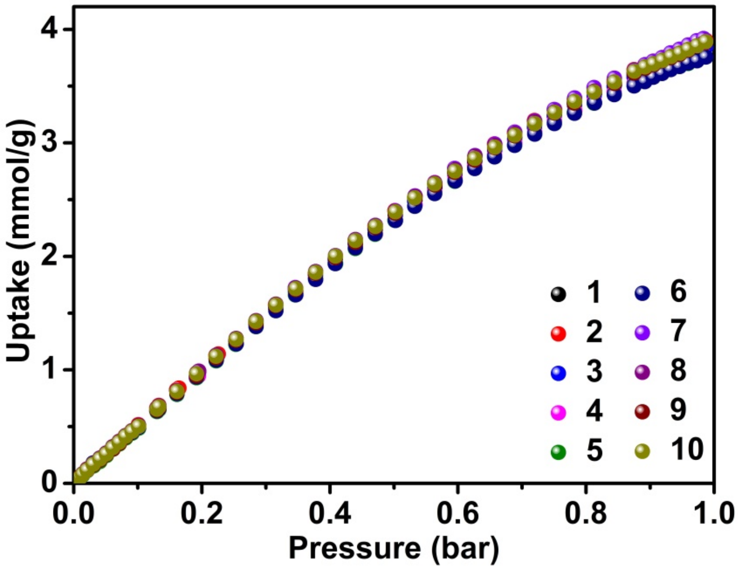

Fig. S23 Continuous C_2H_4 adsorption measurements on JNU-6-CH_3 at 298 K.

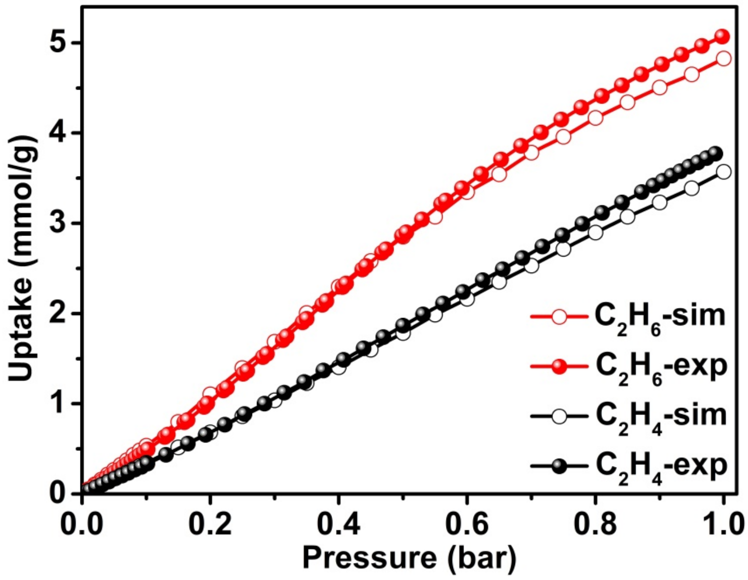

Fig. S24 Experimental and simulated adsorption isotherms of JNU-6 for C_2H_6 (red) and C_2H_4 (black) at 298 K (0-1 bar).

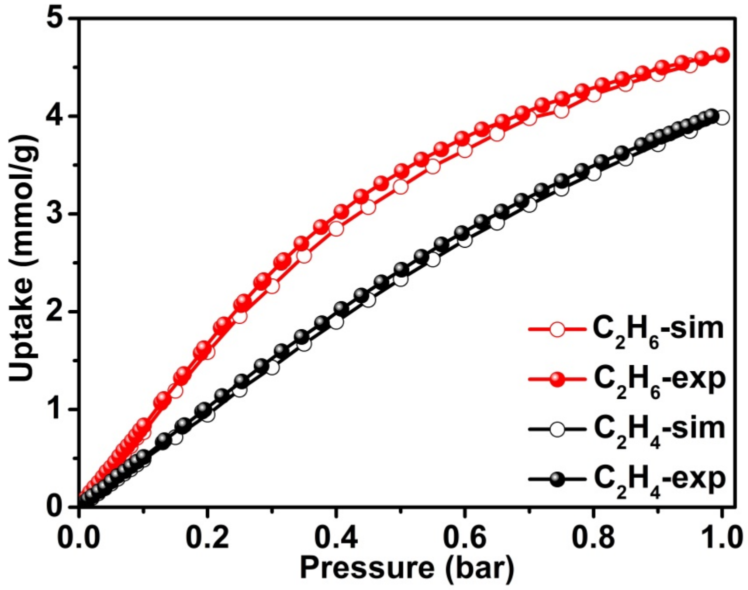

Fig. S25 Experimental and simulated adsorption isotherms of JNU-6-CH_3 for C_2H_6 (red) and C_2H_4 (black) at 298 K.

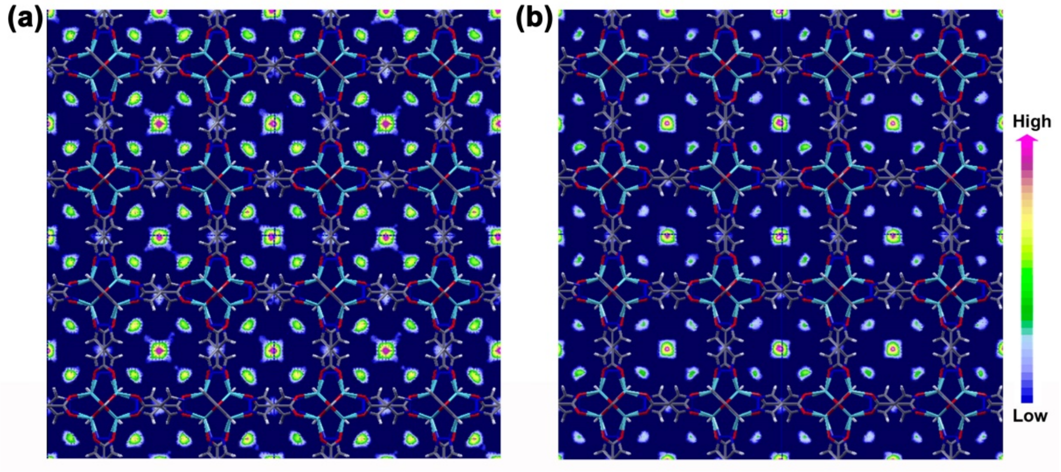

Fig. S26 Contour plots of the COM probability density distributions of (a) C_2H_6 and (b) C_2H_4 for the adsorbed in JNU-6 at 298 K and 1.0 bar. The MOF structure is displayed in a stick style for clarity (atom colors: Zn, cyan; O, red; N, blue; C, gray; H, white).

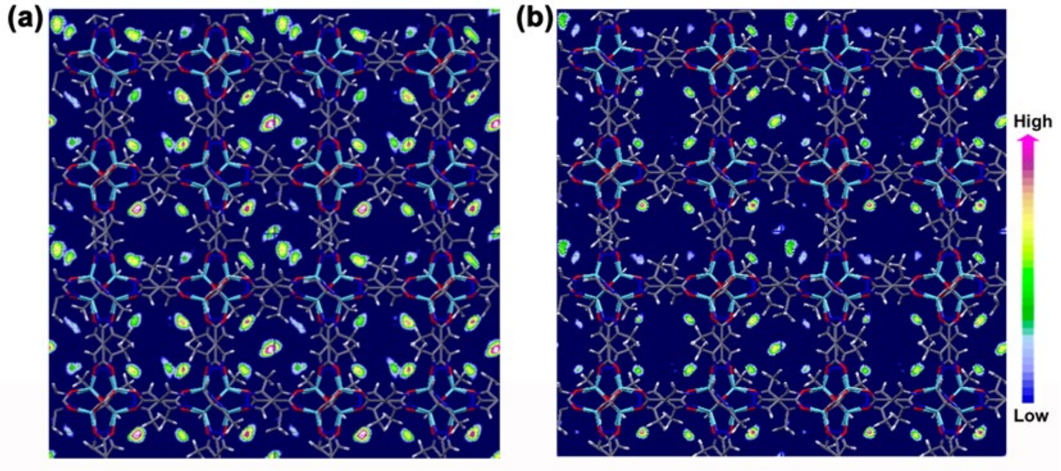

Fig. S27 Contour plots of the COM probability density distributions of (a) C_2H_6 and (b) C_2H_4 for the adsorbed in JNU-6-CH_3 at 298 K and 1.0 bar. The MOF structure is displayed in a stick style for clarity (atom colors: Zn, cyan; O, red; N, blue; C, gray; H, white).

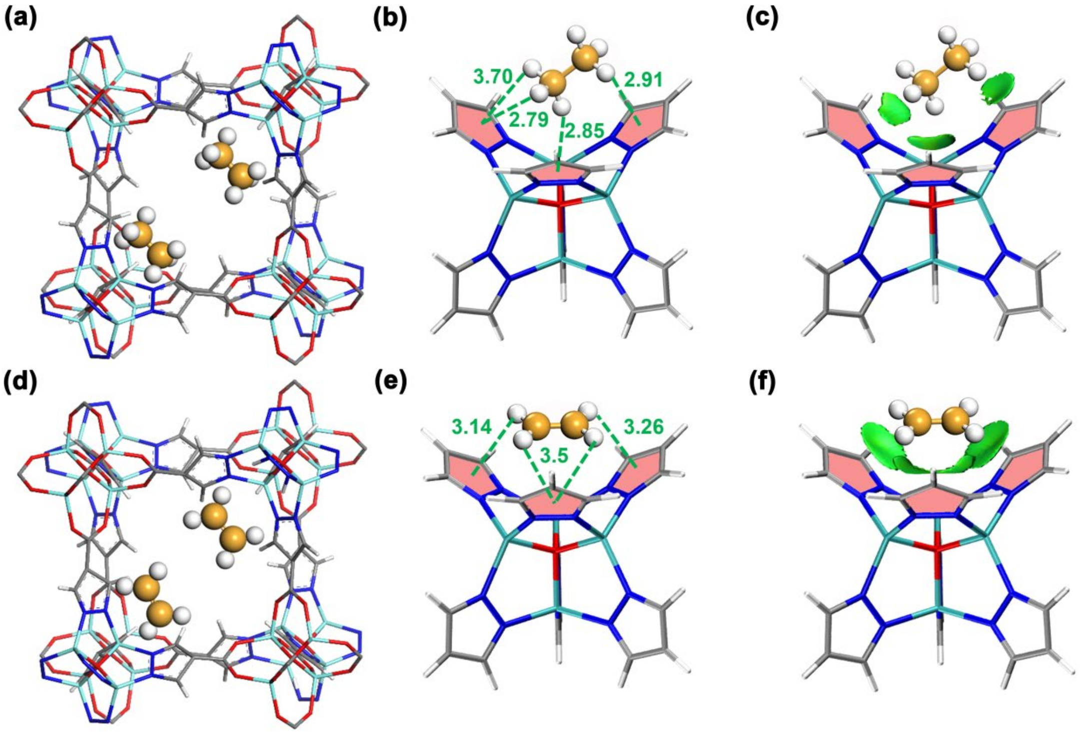

Fig. S28 Primary adsorption sites for C_2H_6 (a) and C_2H_4 (d) in JNU-6 determined by Monte Carlo (GCMC) simulations. C–H···π interactions (green dashed lines) for C_2H_6 (b) and C_2H_4 (e) at the adsorption site of JNU-6. Independent gradient model based on Hirshfeld partition (IGMH) for C_2H_6 (c) and C_2H_4 (f) at the adsorption site of JNU-6 (green surfaces represent vdW interactions). (Color code: Zn, cyan; C, dark gray; N, blue; O, red; H, white. The distance unit is Å).

Table S4. The calculated intermolecular interaction energy between gases and JNU-6 serials of materials.

Parameter	**ΔE (C_2H_6) kJ/mol**	**ΔE (C_2H_4) kJ/mol**
JNU-6	-18.04	-17.22
JNU-6-CH_3	-22.23	-20.15

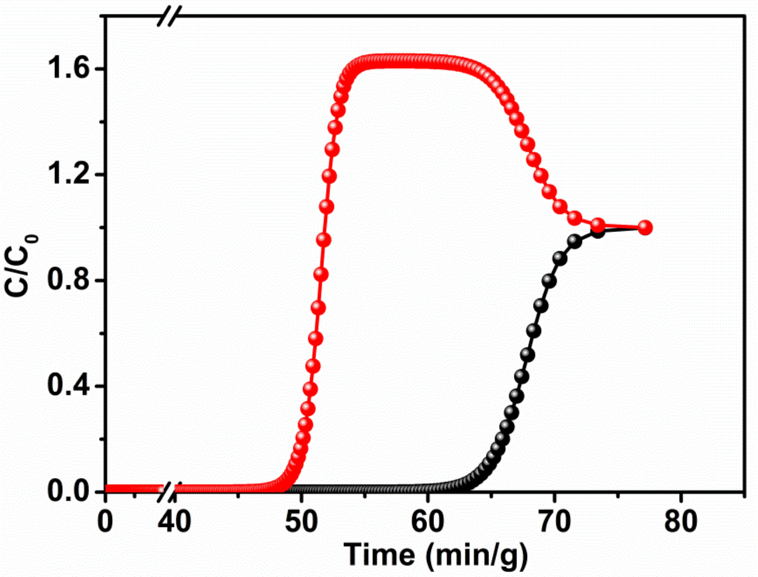

Fig. S29 Transient breakthrough curves for the C_2H_6/C_2H_4 (50:50) mixture in the fixed bed packed with JNU-6-CH_3 at 298 K and 1 bar.

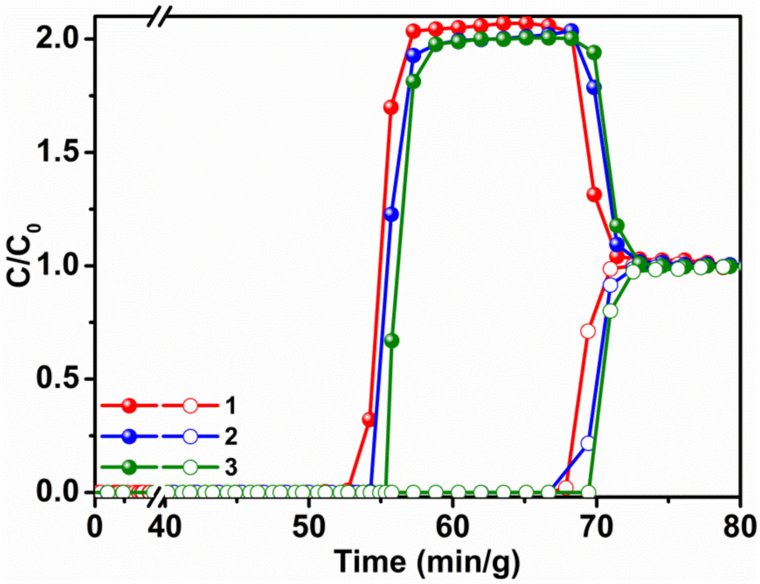

Fig. S30 Three cycles of breakthrough experiments on JNU-6-CH_3 for a C_2H_6/C_2H_4 (50/50, v/v) mixture at a flow rate of 2.0 mL min^{-1} and 298 K under 0% RH conditions.

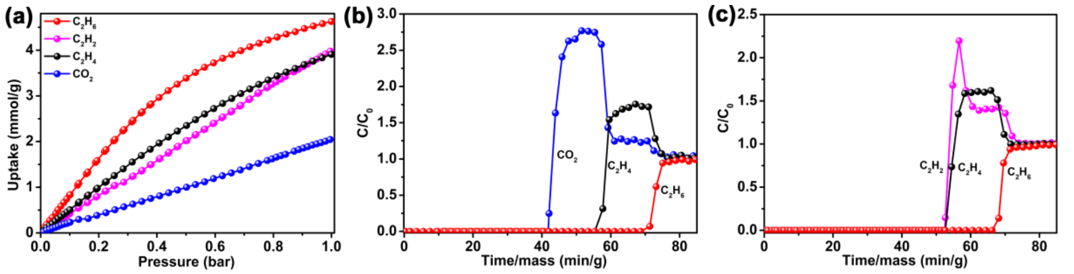

Fig. S31. (a) C_2H_6, C_2H_4, C_2H_2, and CO_2 adsorption isotherms of JNU-6-CH_3 at 298 K. (b) Experimental breakthrough curves of JNU-6-CH_3 (0.70 g) for a $C_2H_6/C_2H_4/CO_2$ (1/1/1, v/v/v) mixture at a flow rate of 2.0 mL min^{-1} and 298 K. (c) Experimental breakthrough curves of JNU-6-CH_3 (0.70 g) for a $C_2H_6/C_2H_4/C_2H_2$ (1/1/1, v/v/v) mixture at a flow rate of 2.0 mL min^{-1} and 298 K. Based on the breakthrough curves, the relative adsorption selectivities of JNU-6-CH_3 were estimated to be 1.7/1.3/1, and 1.3/1.03/1 for $C_2H_6/C_2H_4/CO_2$ (1/1/1, v/v/v), and $C_2H_2/C_2H_4/C_2H_6$ (1/1/1, v/v/v) at 298 K, respectively.

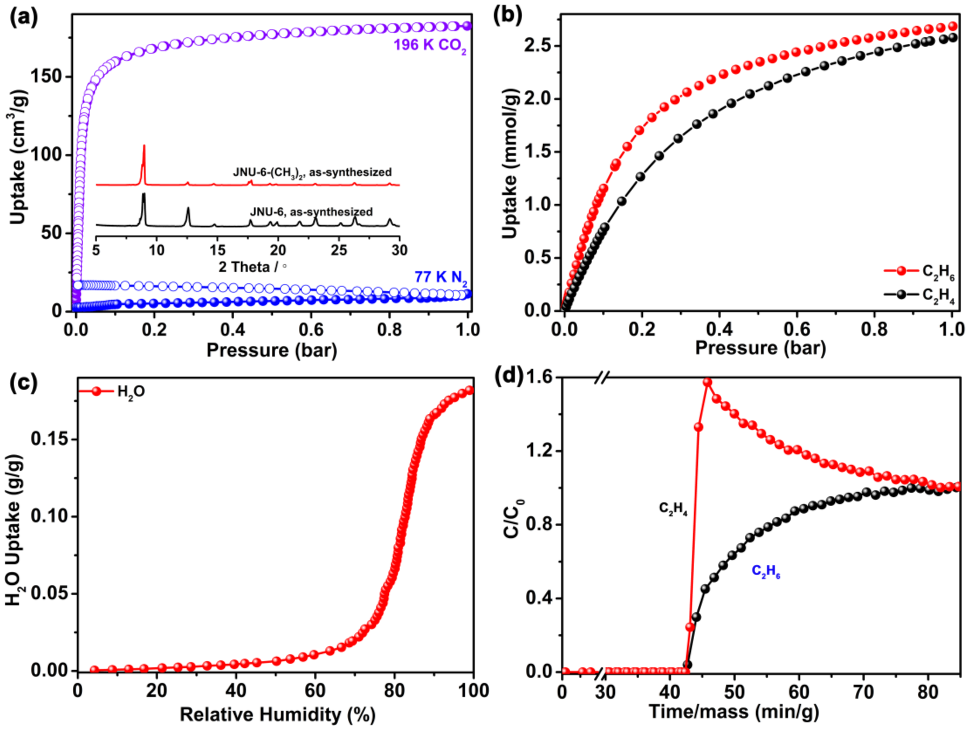

Fig. S32 (a) N_2 and CO_2 adsorption isotherms of JNU-6-$(CH_3)_2$ at 77 K and 196 K respectively. Inset shows the PXRD patterns of the as-synthesized of JNU-6 and JNU-6-$(CH_3)_2$. (b) C_2H_6 and C_2H_4 adsorption isotherms of JNU-6-$(CH_3)_2$ at 298 K (c) Water vapor adsorption isotherm of JNU-6-$(CH_3)_2$ at 298 K. (d) Experimental breakthrough curves on JNU-6-$(CH_3)_2$ (0.92 g) for a C_2H_6/C_2H_4 (50/50, v/v) mixture at a flow rate of 2.0 mL min^{-1} and 298 K under 0% RH conditions.

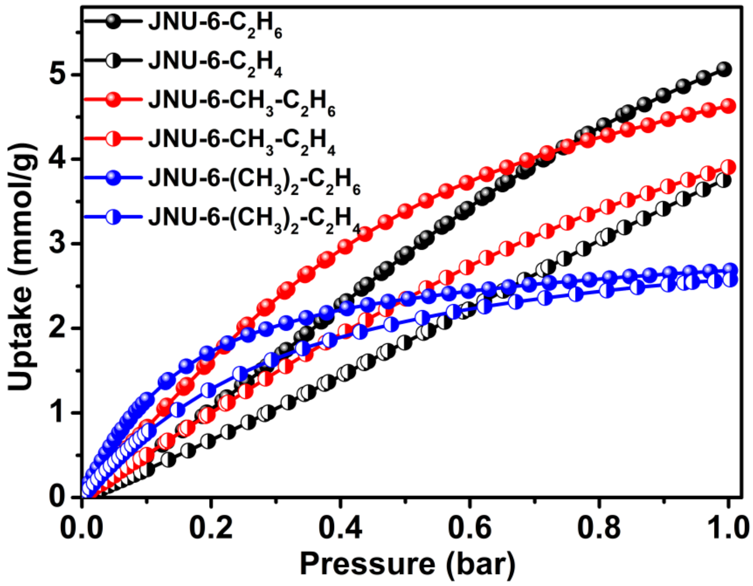

Fig. S33 C_2H_6 and C_2H_4 adsorption isotherms of JNU-6, JNU-6-CH_3, and JNU-6-$(CH_3)_2$ at 298 K.

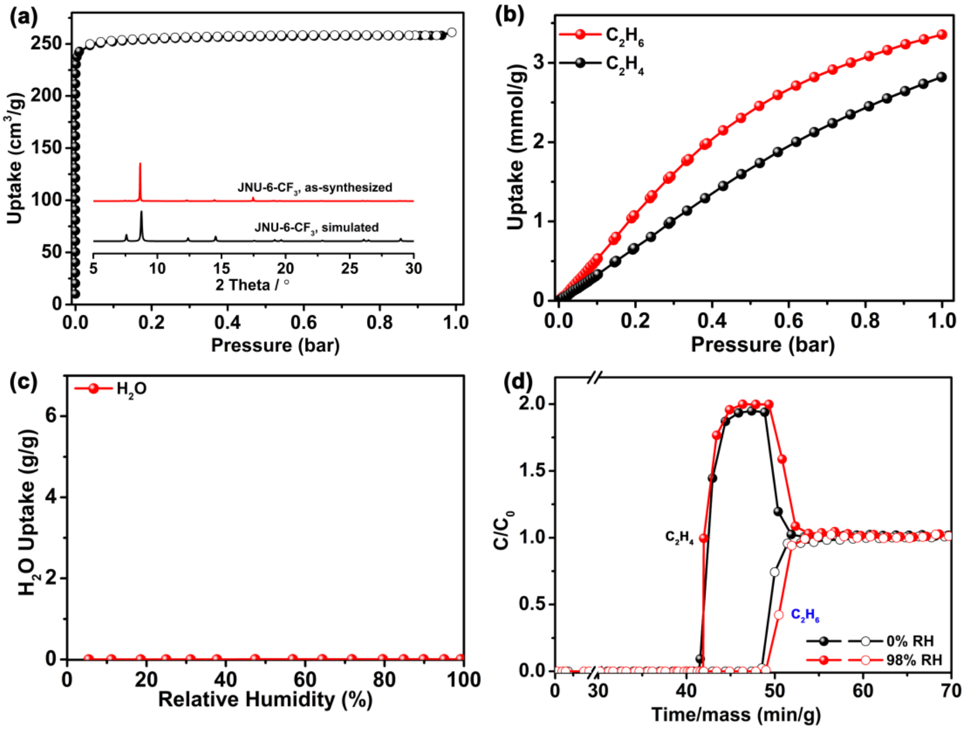

Fig. S34 (a) N_2 adsorption/desorption isotherms of JNU-6-CF_3 at 77 K. Inset shows the PXRD patterns of the as-synthesized and simulated for JNU-6-CF_3. (b) C_2H_6 and C_2H_4 adsorption isotherms of JNU-6-CF_3 at 298 K. (c) Water vapor adsorption isotherm of JNU-6-CF_3 at 298 K. (d) Experimental breakthrough curves of JNU-6-CF_3 (0.9 g) for a C_2H_6/C_2H_4 (50/50, v/v) mixture at a flow rate of 2.0 mL min^{-1} and 298 K under dry or 98% RH conditions. Based on the breakthrough curves, the relative adsorption selectivity of JNU-6-CH_3 was estimated to be 1.3/1 for C_2H_6/C_2H_4 (1/1, v/v).

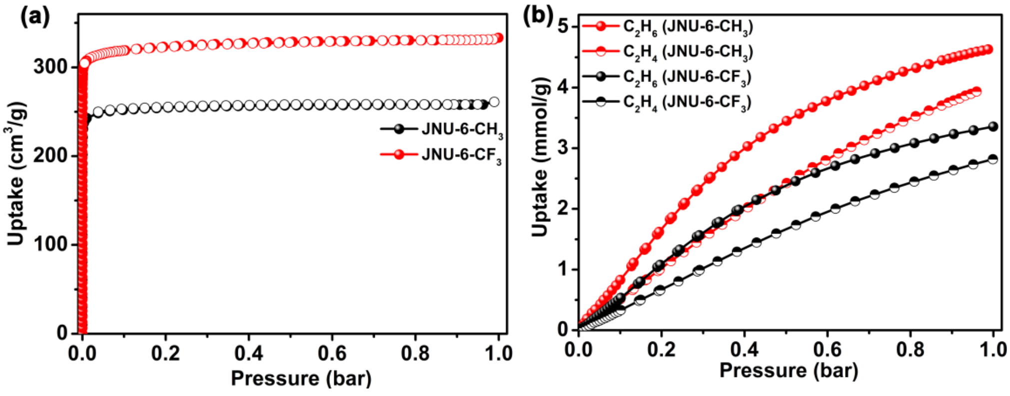

Fig. S35 (a) N_2 adsorption/desorption isotherms of JNU-6-CH_3 and JNU-6-CF_3 at 77 K. (b) C_2H_6 and C_2H_4 adsorption isotherms of JNU-6-CH_3 and JNU-6-CF_3 for at 298 K.

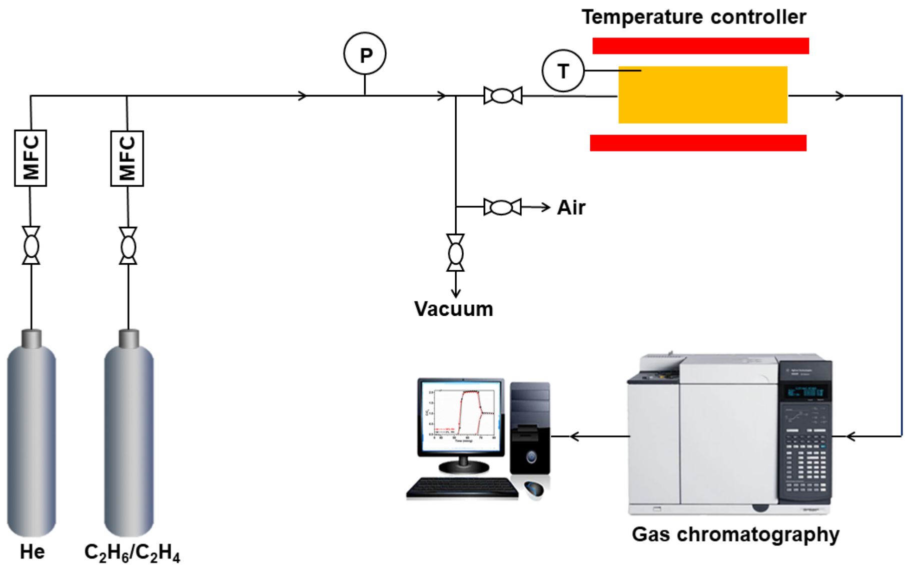

Fig. S36 Schematic illustration of the setup for breakthrough experiments.

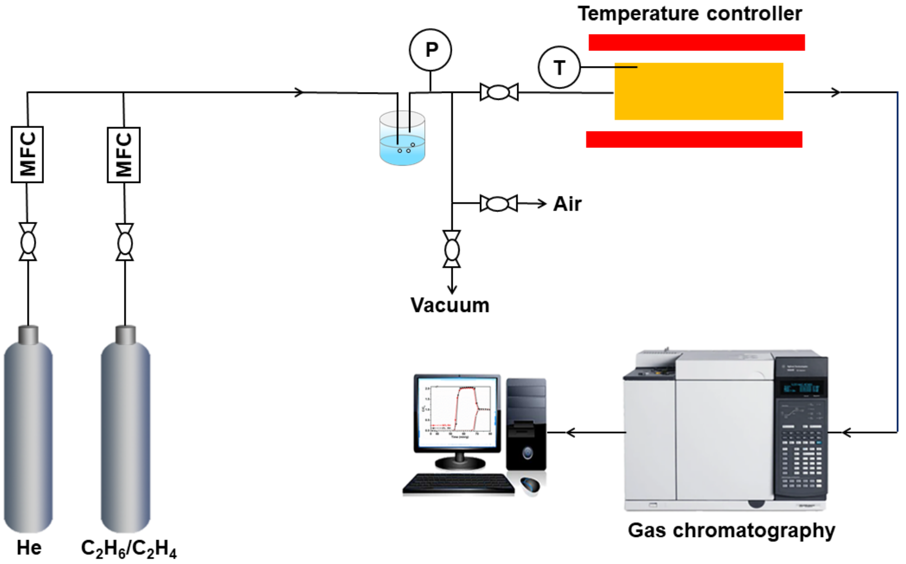

Fig. S37 Schematic illustration of the apparatus for the breakthrough experiments under humid conditions.

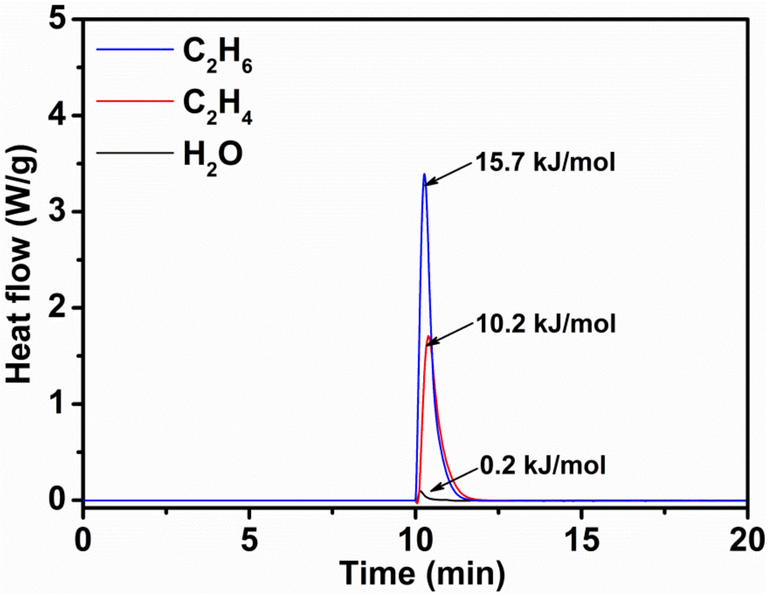

Fig. S38. Differential scanning calorimetry (DSC) for the adsorption of C_2H_6**,** C_2H_4 and **H_2O** on JNU-6 at 298 K and 1 bar.

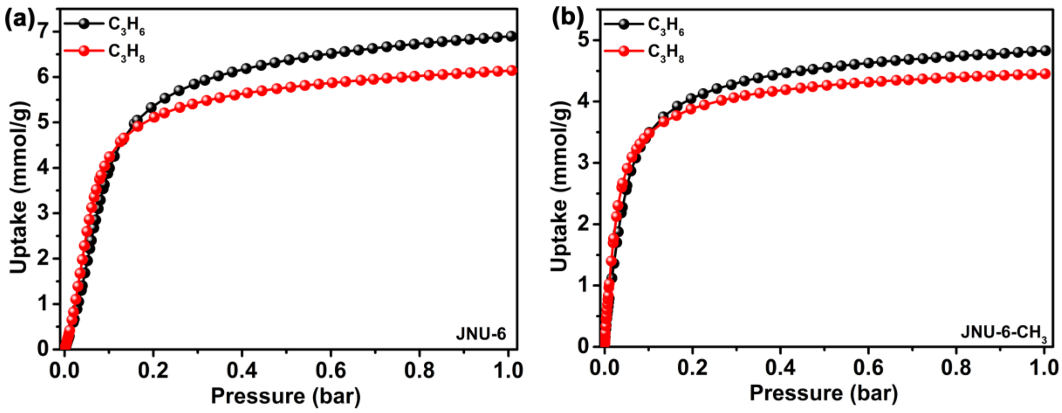

Fig. S39. C_3H_6 and C_3H_8 adsorption isotherms of JNU-6 and JNU-6-CH_3 at 298 K.

Table S5. Crystal data of JNU-6 JNU-6-CH_3 and JNU-6-CF_3.

	JNU-6	JNU-6-CH_3	JNU-6-CF_3
Formula	$C_4H_2N_{2.3}Zn$	$C_5H_4N_{2.25}Zn$	$C_{4.5}HF_3N_{2.25}Zn$
CCDC number	2259108	2258075	2286047
Space group	$Fm\bar{3}c$	$Fm\bar{3}c$	$Fm\bar{3}c$
Crystal system	cubic	cubic	cubic
a (Å)	20.11	20.15	20.18
b (Å)	20.11	20.15	20.18
c (Å)	20.11	20.15	20.18
α (deg)	90	90	90
β (deg)	90	90	90
γ (deg)	90	90	90
V $(Å)^3$	8140.9 (4)	8184.52 (17)	8226.3 (3)
Z	1	1	1
ρ calcg/cm^3	1.172	1.256	1.599
μ/mm^{-1}	3.019	3.039	3.604
Final R	R1= 6.77	R1= 5.52	R1=6.42
[I>2 sigma (I)]	wR1=19.84	wR1=15.27	wR1=17.86
GooF	1.099	1.098	1.113
Completeness	100%	100%	100%

Table S6. Comparison of adsorption capacity, selectivity, and Q_{st} for some selected MOFs.

MOFs	**C_2H_6 uptake (mmol/g)**	**C_2H_4 uptake (mmol/g)**	**C_2H_6/C_2H_4 Selectivity**	**Q_{st} C_2H_6/C_2H_4 (kJ/mol)**	**Ref**
JNU-6	5.07	3.77	1.94	17.7/15.7	This work
JNU-6-CH_3	4.63	3.93	2.27	21.2/20.2	This work
NKMOF-8-Br	4.22	3.67	2.65	40.8/33.6	31
NKMOF-8-Me	4.82	4.67	1.88	38.4/37.6	31
Cu $(Qc)_2$	1.85	0.78	3.4	29/25.4	32
IRMOF-8	3.6	2.75	1.6	52.5/50	33
MAF-49	1.72	1.69	2.7	61/48	34
ZIF-7	2.0	1.82	1.5	-/-	35
$Fe_2(O_2)$ (dobdc)	3.4	2.6	4.4	66.8/36.5	36
CPM-733	7.1	6.3	1.75	23.4/22.5	37
JNU-2	4.1	3.6	1.6	29.4/26.7	38
NPU-2	4.42	3.42	1.52	19.6/18.2	39
MUF-15	4.69	4.15	1.96	29.2/28.2	40
MCIF-1	2.4	2.19	1.61	30/29	41
TJT-100	3.66	3.4	1.2	29/25	42
Zn-atz-ipa	1.81	1.8	1.7	45.8/40	43
Ni $(IN)_2$	3.05	0.89	2.44	34.5/33.3	44
AzoleTh-1	4.47	3.62	1.46	28.6/26.1	45
Tb-MOF-76(NH_2)	3.27	2.97	2.05	32.8/22.4	46
FJI-H11-Me(des)	2.59	2.05	2.09	38.9/25.9	47
1a	3.63	3.28	2.15	31.8/23.2	48
UIO-67-$(NH_2)_2$	5.32	4.32	1.7	26.5/24.5	49
Zn-atz-oba	2.1	2	1.27	30/27	50

References

1. A. L. Myers, J. M. Prausnitz, *A.I.Ch.E.J.* 1965, **11**, 121-130.
2. D. Dubbeldam, A. Torres-Knoop, K. S. Walton, *Mol. Simul.*, 2013, **39**, 1253-1292.
3. D. Dubbeldam, S. Calero, D. E. Ellis, R. Q. Snurr, *Mol. Simul.*, 2016, **42**, 81-101.
4. S. L. Mayo, B. D. Olafson, W. A. Goddard, *J. Phys. Chem.*, 1990, **94**, 8897-8909.
5. A. K. Rappé, C. J. Casewit, K. S. Colwell, W. A. Goddard, W. M. Skiff, UFF, *J. Am. Chem. Soc.*, 1992, **114**, 10024-10035.
6. D. Dubbeldam, S. Calero, T. J. H. Vlugt, R. Krishna, T. L. M. Maesen, B. Smit, *J. Phys. Chem. B.*, 2004, **108**, 12301-12331.
7. S. Ban, A. V. Laak, P. E. Jongh, J. P. J. M. Eerden, T. J. H. Vlugt, *J. Phys. Chem. C.*, 2007, **111**, 17241-17248.
8. T. A. Manz, D. S. Sholl, *J. Chem. Theory. Comput.*, 2010, **6**, 2455-2468.
9. G. Kresse, J. Furthmuller, Phys. Rev. B: Condens. *Matter Mater. Phys.*, 1996, **54**, 11169-11186.
10. G. Kresse, D. Joubert, Phys. Rev. B: Condens. *Matter Mater. Phys.*, 1999, **59**, 1758-1775.
11. A. D. Becke, *J. Chem. Phys.*, 1992, **96**, 2155-2160.
12. S. Grimme, J. Antony, S. Ehrlich, H. Krieg, *J. Chem. Phys.*, 2010, **132**, 154104.
13. P. C. Hariharan, J. A. Pople, *Theoretica. Chimica. Acta.*, 1973, **28**, 213-222.
14. L. E. Roy, P. J. Hay, R. L. Martin, *J. Chem. Theory. Comput.*, 2008, **4**, 1029-1031.
15. S. F. Boys, F. Bernardi, *Mol. Phys.*, 1970, **19**, 553-566.
16. M. J. Frisch, G. W. Trucks, H. B. Schlegel, G. E. Scuseria, M. A. Robb, J. R. Cheeseman, G. Scalmani, V. Barone, G. A. Petersson, H. Nakatsuji, Gaussian 16, revision B.01; Gaussian, Inc.: Wallingford, CT, 2016. **66**.
17. J. S. Murray, P. Politzer, Electrostatic potentials: chemical applications. In: Schleyer PvR (ed) Encyclopedia of computational chemistry. Wiley, West Sussex, pp 1998, 912-920.
18. J. Zhang, T. Lu, *Phys. Chem. Chem. Phys.*, 2021, **23**, 20323.
19. T. Lu, Q. J. Chen, *J. Comput. Chem.*, 2022, **43**, 539-555.
20. T. Lu, F. W. Chen, *J. Comput. Chem.*, 2012, **33**, 580-592.
21. W. Humphrey, A. Dalke, K. Schulten, VMD: Visual molecular dynamics, *J. Mol. Graphics.*, 1996, **14**, 33-38.

22. J. Liu, J. Tian, P. K. Thallapally, B. P. McGrail, *J. Phys. Chem. C.*, 2012, **116**, 9575-9581.
23. R. Krishna, *RSC Adv.* **2017**, 7, 35724-35737.
24. R. Krishna, *ACS Omega* **2020**, 5, 16987−17004.
25. R. Krishna, *Microporous Mesoporous Mater.* **2014**, *185*, 30-50.
26. R. Krishna, *RSC Adv.* **2015**, *5*, 52269-52295.
27. R. Krishna, *Sep. Purif. Technol.* **2018**, *194*, 281-300.
28. S. Q. Yang, T. L. Hu. *Coord. Chem. Rev.*, 2022, **468**, 214628.
29. C. Graham, J. Pierrus, R. E. Raab, *Mol. Phys.*, 1989, **67**, 939-955.
30. J. Zhang, T. Lu, *Phys. Chem. Chem. Phys.*, 2021, **23**, 20323-2032.
31. S. B. Geng, E. Lin, X. Li, *J. Am. Chem. Soc.*, 2021, **143**, 8654-8660.
32. R. B. Lin, H. Wu, L Li, X. L. Tang, Z. Li, J. Gao, H. Cui, W. Zhou, B. L. Chen, *J. Am. Chem. Soc.*, 2018, **140**, 12940-12946.
33. J. Pires, M. L. Pinto, V. K. Saini, *ACS Appl. Mater. Interfaces.*, 2014, **6**, 12093-12099.
34. P. Q. Liao, W. X. Zhang, J. P. Zhang, X. M. Chen, *Nat. Commun.*, 2015, **6**, 8697-8705.
35. C. Gucuyener, J. Van den Bergh, J. Gascon, F. Kapteijn, *J. Am. Chem. Soc.*, 2010, **132**, 17704-17706.
36. L. Li, R.-B Lin, R. Krishna, H. Li, S. Xiang, H. Wu, J. Li, W. Zhou, B. Chen, *Science.*, 2018, **362**, 443-446.
37. H. J. Yang, Y. X. Wang, R. Krishna, X. X. Jia, Y. Wang, A. N. Hong, C. Dang, H. E. Castillo, X. H. Bu, P. Y. Feng, *J. Am. Chem. Soc.*, 2020, **142**, 2222-2227.
38. H. Zeng, X. J. Xie, M. Xie, Y. L. Huang, D. Luo, T. Wang, Y. Zhao, W. Lu, D. Li, *J. Am. Chem. Soc.*, 2019, **141**, 20390-20398.
39. B. Zhu, J. Cao, S. Mukherjee, T. Pham, T. Zhang, T. Wang, X. Jiang, K. A. Forrest, M. J. Zaworotko, K. *J. Am. Chem. Soc.*, 2021, **143**, 1485-1492.
40. O. T. Qazvini, R. Babarao, Z-L. Shi, Y-B. Zhang, S. G. Telfer, *J. Am. Chem. Soc.*, 2019, **141**, 5014-5020.
41. N. Zhao, P. Li, X. Mu, C, Liu, F. Sun, G. Zhu, *Faraday. Discuss.*, 2017, **201**, 63-70.
42. H. G. Hao, Y. F. Zhao, D. M. Chen, J. M. Yu, K. Tan, S. Q. Ma, Y. Chabal, Z. M. Zhang, J. M. Dou, Z. H. Xiao, G. Day, H. C. Zhou, T. B. Lu, *Angew. Chem. Int. Ed.*, 2018, **57**, 16067-16071.

43. K. J. Chen, D. G. Madden, S. Mukherjee, T. Pham, K. A. Forrest, A. Kumar, B. Space, J. Kong, Q. Y. Zhang, M. J. Zaworotko, *Science*, 2019, **366**, 241-246.
44. M. Kang, S. Yoon, S. Ga, D.W. Kang, S. Han, J.H. Choe, H. Kim, D.W. Kim, Y.G. Chung, C.S. Hong, *Adv. Sci.*,2021, **8**, 2004940.
45. Z. Xu, X. Xiong, J. Xiong, R. Krishna, L. Li, Y. Fan, F. Luo, B. Chen, *Nat. Commun.*, 2020, **11**, 3163.
46. G. D. Wang, R. Krishna, Y. Z. Li, W. J. Shi, L. Hou, Y. Y. Wang, Z. H. Zhu, *Angew. Chem. Int. Ed.*, 2022, **61**, e202213015.
47. Z. Y. Di, C. P. Liu, J. D Pang, S. X. Zou, Z. Y. Ji, F. L. Hu, C. Chen, D. Q. Yuan, M. C. Hong, M. Y. Wu, *Angew. Chem. Int. Ed.*,2022, **61**, e202210343.
48. G. D. Wang, Y. Z. Li, W. J. Shi, L. Hou, Y. Yu. Wang, Z. H. Zhu, *Angew. Chem. Int. Ed.*, 2022, **61**, e202205427.
49. X.W. Gu, J. X. Wang, E. Wu, H. Wu, W. Zhou, G. Qian, B. Chen, B. Li, *J. Am. Chem. Soc.*, 2022, **144**, 2614-2623.
50. J. W. Cao, S. Mukherjee, T. Pham, Y. Wang, T. Wang, T. Zhang, X. Jiang, H. J. Tang, K. A. Forrest, B. Space, M. J. Zaworotko, K.-J. Chen, *Nat. Commun.*, 2021, **12**, 6507.